

Supplementary Information for “Magnetic miniature actuators with six-DOF multimodal soft-bodied locomotion”

Changyu Xu¹, Zilin Yang¹, Shaun Wee Kiat Tan¹, Jianhuang Li¹, and Guo Zhan Lum¹

¹Affiliation not available

December 30, 2021

Abstract

This Supplementary Information includes:

Section S1- Fabrication method

Section S2- Actuation method

Section S3- Analysis of sixth-DOF torque

Section S4- Experiments

Figures S1-S31

Supporting Table

References

Other supplementary materials for this manuscript include the following:

Supporting SI Videos S1-S10

Corresponding author(s) Email: gzlum@ntu.edu.sg

Section S1- Fabrication method

In this section, we would first elaborate on the fabrication process of our proposed soft MMR (section S1A). Subsequently, we discussed about the experiments that evaluated the proposed MMR’s material properties (section S1B).

A. Fabrication of six-DOF soft MMR

The detailed dimensions of our six-DOF MMR could be found in Fig. S1. To fabricate the proposed MMR, we first constructed its magnetic soft beam component. This soft component was molded by embedding hard magnetic microparticles (NdFeB, average diameter: 5 μm) into the liquid polymer matrix (Ecoflex 00-10) with a 4:1 mass ratio. The mixture was then cured in an oven for two hours at 80 $^{\circ}\text{C}$. Once the beam was molded (Fig. S2A), it was rolled in a cylindrical jig and subsequently magnetized by a strong, uniform magnetic field of 1.1 T (Fig. S2B). After this magnetization process, the magnetized beam would be endowed with its desired harmonic magnetization profile (\vec{M} , $\varphi = 90^{\circ}$) after it recovered to its original configuration (Fig. S2C). Two identical buoyant components, made from Styrofoam and cut to their desired geometry, were each adhesively bonded to the free ends of the magnetic soft beam to form the proposed MMR (Fig.

S1). For the experiment in Fig. 6D, the buoyant components were also coated with a thin layer of Ecoflex 00-10 to make their surfaces hydrophobic.

B. Characterization of the magnetic soft beam's material properties

Here we conducted a simple experiment to evaluate the $|\vec{M}|$ of our magnetic soft beam. Five cuboid samples were constructed by the same material used for fabricating our magnetic soft beam, and these samples had the following dimensions: 6 mm length (L_{sp}), 4 mm width (w_{sp}) and 1 mm thickness (t_{sp}) (Fig. S3A). The samples were magnetized by a strong, uniform magnetic field of 1.1 T along their length, and their weights (W) were measured by a high-precision weighing scale (A&D GH-120). Different rotary equilibrium states could be established when the samples were subjected to a \vec{B} , which was inclined at 45° from the horizontal plane, with varying magnitudes from 4 mT to 6 mT (Fig. S3B). As the rigid-body torque induced by the samples' weight would make the net magnetic moment of the samples (\vec{m}_{sp}) misalign with the applied \vec{B} , we could use a camera to record the misalignment angle, \varnothing , between \vec{m}_{sp} and \vec{B} (Fig. S3B). By performing a torque equilibrium analysis on the samples (Fig. S3B), the following governing equation could be obtained:

$$|\vec{m}_{sp}| |\vec{B}| \sin \varnothing = W r_0 \cos \Gamma,$$

where

$$r_0 = \frac{\sqrt{L_{sp}^2 + t_{sp}^2}}{2}. \quad (S1.1)$$

The parameter r_0 represented the distance between the samples' center of mass and anchor point, and Γ represented the angle between the inclined samples and the substrate (Fig. S3B). Since the samples' $|\vec{M}|$ could be computed as $\frac{|\vec{m}_{sp}|}{V_{sp}}$, where V_{sp} represented the volume of the cuboid samples, we could rearrange Eq. (S1.1) to evaluate $|\vec{M}|$:

$$\frac{W r_0 \cos \Gamma}{V_{sp} \sin \varnothing} = |\vec{M}| |\vec{B}|. \quad (S1.2)$$

Using Eq. (S1.2), we plotted $\frac{W r_0 \cos \Gamma}{V_{sp} \sin \varnothing}$ against $|\vec{B}|$ to determine the experimentally obtained $|\vec{M}|$ via the gradient of the best fit line of these data (Fig. S3C). Using this analysis, we evaluated the $|\vec{M}|$ of our material to be $9.40 \times 10^4 \text{ A m}^{-1}$ when it was magnetized by a 1.1 T magnetic field.

In addition, we also evaluated the Young's modulus of the magnetic soft beam to be $271 \pm 11.7 \text{ kPa}$ via a standard compression test (SHIMADZU AG-X plus, 10 kN).

Section S2- Actuation method

In this section, we will discuss the actuation principles of our proposed MMR. Specifically, we will derive the deformation mechanism of the MMR (section S2A), analyze its six-DOF motions (section S2B), and include additional discussions (section S2C). For these analyses, we assume that the applied \vec{B} and its spatial gradients are uniform across the MMR's body as it is difficult to spatially vary these control signals

at small scale (Diller et al., 2016; Kummer et al., 2010; Diller et al., 2014). Furthermore, due to Gauss’s law and Ampere’s law (assuming no electric currents flowing in the workspace), we also include the following constraints on the spatial gradients of \vec{B} (Diller et al., 2016; Xu et al., 2021):

$$\frac{\partial B_x}{\partial x} + \frac{\partial B_y}{\partial y} + \frac{\partial B_z}{\partial z} = 0, (S2.1A)$$

$$\frac{\partial B_z}{\partial x} = \frac{\partial B_x}{\partial z}, \quad \frac{\partial B_z}{\partial y} = \frac{\partial B_y}{\partial z}, \quad \frac{\partial B_y}{\partial x} = \frac{\partial B_x}{\partial y}. (S2.1B)$$

Equation (S2.1) is valid across all the reference frames, and it dictates that there are only five independent spatial gradients of \vec{B} . To facilitate our subsequent discussions, we will represent \vec{B}_{grad} with the following format:

$$\vec{B}_{\text{grad}} = \left[\frac{\partial B_z}{\partial x} \quad \frac{\partial B_z}{\partial y} \quad \frac{\partial B_z}{\partial z} \quad \frac{\partial B_y}{\partial y} \quad \frac{\partial B_x}{\partial y} \right]^T. (S2.2)$$

A. Deformation mechanism

In comparison, the buoyant components are much more rigid than the magnetic beam component, and thus the deformation mechanism of the proposed MMR is mainly contributed by the magnetic beam. As a result, here we would only derive the theoretical quasi-static model that describes the deformation characteristics of the beam, and we assume that the buoyant components are rigid.

According to the materials reference frame (Fig. 1A(ii)), the harmonic magnetization profile ($\vec{M}_{\{M\}}$) of the beam along its length, s , can be expressed mathematically as:

$$\vec{M}_{\{M\}}(s) = \left| \vec{M}_{\{M\}} \right| \left(0, \quad amp; \cos \left(-\frac{2\pi}{L}s - \frac{\pi}{2} \right), \quad amp; \sin \left(-\frac{2\pi}{L}s - \frac{\pi}{2} \right) \right)^T, (S2.3)$$

where L represents the total length of the beam. In general, $\vec{M}_{\{M\}}$ can be approximated as a collection of magnetic dipoles that are embedded in the MMR’s magnetic beam component (Xu et al., 2021). By applying \vec{B} along the $z_{\{L\}}$ -axis, the interaction of $\vec{M}_{\{M\}}(s)$ and the applied magnetic field will generate a distribution of magnetic torque (per unit volume) along the magnetic beam, $\tau_{x,\{L\}}(s)$, which will in turn deform the MMR. The deformation of the magnetic soft beam can be represented mathematically by its rotational deflection, $\gamma(s)$ (Fig. S4).

By performing a quasi-static analysis on an arbitrary infinitesimal element of the magnetic beam (Fig. S4), the torque equilibrium equation, according to the local reference frame, can be derived as:

$$-\tau_{x,\{L\}}(s) Ads = \frac{\partial M_b}{\partial s}(s) ds, (S2.4)$$

where M_b and A represent the bending moment applied at sand the corresponding cross-sectional area of the beam, respectively. The variable, $\tau_{x,\{L\}}(s)$, on the left side of Eq. (S2.4) can be expanded into (Lum et al., 2016) :

$$\tau_{x,\{L\}}(s) = [1 \quad amp; 0 \quad amp; 0] \left\{ \left(\mathbf{R}_x(\gamma) \vec{M}_{\{M\}}(s) \right) \times \vec{B}_{\{L\}} \right\},$$

where

$$\mathbf{R}_x(\gamma) = \begin{pmatrix} 1 & \text{amp}; 0 & \text{amp}; 0 \\ 0 & \text{amp}; \cos \gamma & \text{amp}; -\sin \gamma \\ 0 & \text{amp}; \sin \gamma & \text{amp}; \cos \gamma \end{pmatrix}. \quad (S2.5)$$

The matrix, \mathbf{R}_x , is the standard rotational matrix about the x -axis, and it is used to account for the change in \vec{M} after the magnetic beam undergoes a large deformation (Lum et al., 2016). Based on the Euler-Bernoulli equation, we can establish the relationship between M_b and γ as (Lum et al., 2016):

$$M_b = EI \frac{\partial \gamma}{\partial s}, \quad (S2.6)$$

where E and I represent the Young's modulus and second moment of inertia of the magnetic beam, respectively. By substituting Eq.s (S2.5) and (S2.6) into Eq. (S2.4), the governing equation that dictates the deformation characteristics of the MMR can be expressed as:

$$- [1 \quad \text{amp}; 0 \quad \text{amp}; 0] \left\{ \left(\mathbf{R}_x(\gamma) \vec{M}_{\{M\}}(s) \right) \times \vec{B}_{\{L\}} \right\} A = EI \frac{\partial^2 \gamma}{\partial s^2}(s). \quad (S2.7)$$

The deformation of the beam, $\gamma(s)$, in Eq. (S2.7) can be solved numerically by using the following free-free boundary conditions: $\frac{\partial \gamma}{\partial s}(s=0) = \frac{\partial \gamma}{\partial s}(s=L) = 0$. Physically, these boundary conditions imply that the MMR will experience zero bending moments at its free ends. Once γ has been solved, the deformed configuration of our MMR will be revealed. For these simulations, Eq. (S2.7) is solved by using the MMR geometries shown in Fig. S1 as well as the following material properties that have been obtained via experimental means (SI section S1B): $|\vec{M}_{\{M\}}| = 9.40 \times 10^4 \text{ A m}^{-1}$ and $E = 271 \text{ kPa}$.

Equations (S2.4-S2.7) indicate that the magnitude of $\vec{B}_{\{L\}}$ has a linear relationship with the bending moment experienced by the magnetic beam. Hence, stronger magnitudes of $\vec{B}_{\{L\}}$ can generally allow our MMR to adopt sharper curvatures (Fig. S5). In general, our numerical solution is able to predict the 'U'- and inverted 'V'-shaped configurations produced by the MMR well. Because the predicted shapes from the simulations agree well with the experimental data (e.g., Fig. 1B), this suggests that the presented derivations can describe the deformation physics of our MMR accurately. This is an important criterion as the curvature of the proposed MMR must be precisely controlled to enable its locomotion. In our derivations, we assume that the distributed magnetic forces along the MMR's magnetic beam component have negligible effects on its deformation. This is because the mechanical stresses induced by the magnetic torques are generally much larger than those generated by the magnetic forces (Xu et al., 2021; Wang et al., 2020). Indeed, we did not observe noticeable deformations on the proposed MMR when magnetic forces were applied to it during the experiments. It is also noteworthy that if the direction of $\vec{B}_{\{L\}}$ is not aligned along the $z_{\{L\}}$ -axis, the MMR will assume the 'U'- or inverted 'V'-shaped configuration and produce a rigid-body rotation until its net magnetic moment, $\vec{m}_{\{L\}}$, is aligned with $\vec{B}_{\{L\}}$, where $\vec{m}_{\{L\}} = \iiint \mathbf{R}_x(\gamma) \vec{M}_{\{M\}} dV$. The variable, V , represents the volume of the beam component of the deformed MMR. We will elaborate on the producible rotations and translations of the MMR in the subsequent sub-section.

B. Six-DOF motion analysis

Based on Eq.s (S2.3) and (S2.7), our undeformed MMR will have a null net magnetic moment, i.e., $\vec{m}_{\{M\}} = \iiint \vec{M}_{\{M\}} dV = \vec{0}_{\{M\}}$. However, once the proposed MMR has assumed its ‘U’- or inverted ‘V’-shaped configuration, it will possess an effective \vec{m} necessary for implementing our six-DOF control, i.e., allowing the MMR to rotate about three axes and translate along three axes. The key concept of our six-DOF actuation strategy is to control the actuating magnetic signals such that the desired orientation of the MMR can become a minimum potential energy configuration. Based on this control strategy, the MMR will constantly experience three axes of restoring torques until it self-aligns to the desired orientation. The restoring torques will also allow the proposed MMR to reject mechanical disturbances such that its desired orientation can be maintained.

When the proposed MMR assumes its deformed ‘U’- or inverted ‘V’-shaped configuration, we can apply \vec{B} and \vec{B}_{grad} to exert magnetic torques and forces on it. Because it will be intuitive to perform such analysis according to the local reference frame of the MMR (Diller et al., 2016; Diller et al., 2014; Xu et al., 2021), we express the net magnetic torque (\vec{T}) and force (\vec{F}) applied on the MMR based on this reference frame (Xu et al., 2021):

$$\begin{aligned} \begin{pmatrix} \vec{T}_{\{L\}} \\ \vec{F}_{\{L\}} \end{pmatrix} &= \begin{pmatrix} \iiint \mathbf{R}_x(\gamma) \vec{M}_{\{M\}} \times \vec{B}_{\{L\}} dV + \iiint \vec{r}_{\{L\}} \times \left(\begin{bmatrix} \frac{\partial \vec{B}_{\{L\}}}{\partial x_{\{L\}}} & \frac{\partial \vec{B}_{\{L\}}}{\partial y_{\{L\}}} & \frac{\partial \vec{B}_{\{L\}}}{\partial z_{\{L\}}} \end{bmatrix}^T \mathbf{R}_x(\gamma) \vec{M}_{\{M\}} \right) dV \\ \iiint (\mathbf{R}_x(\gamma) \vec{M}_{\{M\}} \bullet \nabla) \vec{B}_{\{L\}} dV \end{pmatrix} \\ &= \mathbf{D} \begin{pmatrix} \vec{B}_{\{L\}} \\ \vec{B}_{\text{grad},\{L\}} \end{pmatrix}, \quad (\text{S2.8}) \end{aligned}$$

where \vec{r} represents the displacement vector from the MMR’s center of mass to a point of interest in its body. The matrix \mathbf{D} is known as the design matrix, and it has a 6×8 dimension (Diller et al., 2016; Xu et al., 2021). The design matrix \mathbf{D} of our soft MMR can be explicitly expressed as:

$$\mathbf{D} = \begin{pmatrix} 0 & -|\vec{m}| & 0 & 0 & d_1 & 0 & 0 & 0 \\ |\vec{m}| & 0 & 0 & d_2 & 0 & 0 & 0 & 0 \\ 0 & amp; 0 & d_3 \\ 0 & amp; 0 & amp; 0 & amp; |\vec{m}| & amp; 0 & amp; 0 & amp; 0 \\ 0 & 0 & 0 & 0 & |\vec{m}| & 0 & 0 & 0 \\ 0 & 0 & 0 & 0 & 0 & |\vec{m}| & 0 & 0 \end{pmatrix},$$

$$d_1 = \iiint (r_y M_y - r_z M_z) dV, \quad d_2 = \iiint r_z M_z dV, \quad d_3 = \iiint -r_y M_y dV. \quad (\text{S2.9})$$

The variables, r_y and r_z , represent the Cartesian y - and z -axes components of $\vec{r}_{\{L\}}$. Likewise, the variables, M_y and M_z , represent the Cartesian y - and z -axes components of $\mathbf{R}_x(\gamma) \vec{M}_{\{M\}}$. A notable feature of the \mathbf{D} matrix is that its rank is six (full rank), and this is an important criterion to achieve six-DOF (Diller et al., 2016; Xu et al., 2021).

While it is intuitive to use the local reference frame to analyze the net torque and force applied on the MMR, it is difficult to make the desired orientation of the MMR into a minimum potential energy configuration based on this reference frame (Xu et al., 2021). This is because the local reference frame lacks the information

of the MMR's sixth-DOF angular displacement (θ) (Xu et al., 2021). Therefore, we reanalyze Eq. (S2.8) based on the intermediate reference frame. Specifically, we can use Eq. (2) to reanalyze the left side of Eq. (S2.8) according to the intermediate reference frame:

$$\begin{pmatrix} \vec{T}_{\{I\}} \\ \vec{F}_{\{I\}} \end{pmatrix} = \begin{pmatrix} \mathbf{R}_z(\theta) & \text{amp}; \mathbf{0}_{3 \times 3} \\ \mathbf{0}_{3 \times 3} & \text{amp}; \mathbf{R}_z(\theta) \end{pmatrix} \begin{pmatrix} \vec{T}_{\{L\}} \\ \vec{F}_{\{L\}} \end{pmatrix},$$

where

$$\mathbf{R}_z(\theta) = \begin{pmatrix} \cos \theta & \text{amp}; -\sin \theta & \text{amp}; 0 \\ \sin \theta & \text{amp}; \cos \theta & \text{amp}; 0 \\ 0 & \text{amp}; 0 & \text{amp}; 1 \end{pmatrix}. \quad (\text{S2.10})$$

In a similar way, we can reanalyze the actuating magnetic signals in Eq. (S2.8), according to the intermediate frame, using the following mapping:

$$\begin{pmatrix} \vec{B}_{\{L\}} \\ \vec{B}_{\text{grad},\{L\}} \end{pmatrix} = \mathbf{A} \begin{pmatrix} \vec{B}_{\{I\}} \\ \vec{B}_{\text{grad},\{I\}} \end{pmatrix},$$

where

$$\mathbf{A} = \begin{bmatrix} \cos \theta & \sin \theta & 0 & 0 & 0 & 0 & 0 & 0 \\ -\sin \theta & \cos \theta & 0 & 0 & 0 & 0 & 0 & 0 \\ 0 & 0 & 1 & 0 & 0 & 0 & 0 & 0 \\ 0 & \text{amp}; 0 & \text{amp}; 0 & \text{amp}; \cos \theta & \text{amp}; \sin \theta & \text{amp}; 0 & \text{amp}; 0 & \text{amp}; 0 \\ 0 & \text{amp}; 0 & \text{amp}; 0 & \text{amp}; -\sin \theta & \text{amp}; \cos \theta & \text{amp}; 0 & \text{amp}; 0 & \text{amp}; 0 \\ 0 & 0 & 0 & 0 & 0 & 1 & 0 & 0 \\ 0 & 0 & 0 & 0 & 0 & -\sin^2 \theta & \cos 2\theta & 0 \\ 0 & 0 & 0 & 0 & 0 & 0.5 \sin 2\theta & \sin 2\theta & 0 \end{bmatrix}$$

By substituting Eq.s (S2.10) and (S2.11) into Eq. (S2.8), the mathematical relationship between the wrench and the magnetic signals can be expressed in the intermediate reference frame as:

$$\begin{aligned} \begin{pmatrix} \vec{T}_{\{I\}} \\ \vec{F}_{\{I\}} \end{pmatrix} &= \begin{pmatrix} \mathbf{R}_z(\theta) & \text{amp}; \mathbf{0}_{3 \times 3} \\ \mathbf{0}_{3 \times 3} & \text{amp}; \mathbf{R}_z(\theta) \end{pmatrix} \begin{pmatrix} \vec{T}_{\{L\}} \\ \vec{F}_{\{L\}} \end{pmatrix} \\ &= \begin{pmatrix} \mathbf{R}_z(\theta) & \text{amp}; \mathbf{0}_{3 \times 3} \\ \mathbf{0}_{3 \times 3} & \text{amp}; \mathbf{R}_z(\theta) \end{pmatrix} \mathbf{D} \begin{pmatrix} \vec{B}_{\{L\}} \\ \vec{B}_{\text{grad},\{L\}} \end{pmatrix} \\ &= \begin{pmatrix} \mathbf{R}_z(\theta) & \text{amp}; \mathbf{0}_{3 \times 3} \\ \mathbf{0}_{3 \times 3} & \text{amp}; \mathbf{R}_z(\theta) \end{pmatrix} \mathbf{D} \mathbf{A} \begin{pmatrix} \vec{B}_{\{I\}} \\ \vec{B}_{\text{grad},\{I\}} \end{pmatrix} \end{aligned}$$

where

$$\mathbf{C}(\theta) = \begin{pmatrix} \mathbf{R}_z(\theta) & \text{amp}; \mathbf{0}_{3 \times 3} \\ \mathbf{0}_{3 \times 3} & \text{amp}; \mathbf{R}_z(\theta) \end{pmatrix} \mathbf{D}\mathbf{A}. \quad (\text{S2.12})$$

The matrix $\mathbf{C}(\theta)$ is known as the control matrix (Xu et al., 2021), and it can be expressed explicitly as:

$$\mathbf{C}(\theta) = \begin{pmatrix} 0 & -|\vec{m}| & 0 & d_3 \sin \theta \cos \theta & d_1 \cos^2 \theta - d_2 \sin^2 \theta & 0 \\ |\vec{m}| & 0 & 0 & d_2 \cos^2 \theta - d_1 \sin^2 \theta & -d_3 \sin \theta \cos \theta & 0 \\ 0 & \text{amp}; 0 & \text{amp}; 0 & \text{amp}; 0 & 0 & d_3 \sin \theta \cos \theta \\ 0 & 0 & \text{amp}; 0 & |\vec{m}| & \text{amp}; 0 & 0 \\ 0 & 0 & 0 & 0 & |\vec{m}| & 0 \\ 0 & 0 & 0 & 0 & 0 & |\vec{m}| \end{pmatrix} \text{amp};$$

Since the rank of \mathbf{D} is six, \mathbf{C} would be a full rank matrix too. To make the desired orientation of the MMR into a minimum potential energy configuration, $\vec{T}_{\{I\}}$ is specified to be a null vector when it reaches the desired θ . While the MMR will be in a rotational equilibrium state at its desired orientation, a desired $\vec{F}_{\{I\}}$ can still be applied to the actuator. Based on the desired $\vec{F}_{\{I\}}$, the required magnetic signals necessary for implementing our six-DOF control can be derived by solving Eq. (S2.12):

$$\begin{pmatrix} \vec{B}_{\{I\}} \\ \vec{B}_{\text{grad},\{I\}} \end{pmatrix} = \mathbf{C}^T [\mathbf{C}\mathbf{C}^T]^{-1} \begin{pmatrix} \vec{0}_{3 \times 1, \{I\}} \\ \vec{F}_{\text{desired}, \{I\}} \end{pmatrix} + k_1 \begin{pmatrix} 0 \\ 0 \\ 1 \\ 0 \\ 0 \\ 0 \\ 0 \\ 0 \end{pmatrix}_{\{I\}} + k_2 \begin{pmatrix} 0 \\ 0 \\ 0 \\ 0 \\ 0 \\ 0 \\ 1 \\ -\tan(2\theta) \end{pmatrix}_{\{I\}}. \quad (\text{S2.14})$$

Equation (S2.14) is the general solution of the actuating magnetic signals, and it includes a particular solution obtained via pseudo-inverse (first right-hand component) and the homogeneous solutions formed by the two null space vectors of \mathbf{C} . The variables, k_1 and k_2 , are the scale factors for the null space vectors. Each solution of Eq. (S2.14) has a unique function:

1. The pseudo-inverse solution ensures that the MMR is in a rotational equilibrium state when it reaches the desired orientation, and the desired $\vec{F}_{\{I\}}$ can be applied to the actuator.
2. The first null space vector, $(0 \text{ amp}; 0 \text{ amp}; 1 \text{ amp}; 0 \text{ amp})^T_{\{I\}}$, generates two axes of restoring torques for the MMR, but it cannot generate a restoring torque about the sixth-DOF axis of the actuator (Diller et al., 2016; Kummer et al., 2010; Diller et al., 2014).
3. By adjusting the magnetic actuating signals via the second null space vector, we can generate a restoring torque about the sixth-DOF axis of the MMR (Xu et al., 2021). This restoring torque will in turn allow the MMR's sixth-DOF angular displacement to self-align into its desired θ and subsequently maintain this angle.

In theory, it is ideal to make the strength of the restoring torques in all axes stronger by increasing the magnitudes of k_1 and k_2 in Eq. (S2.14) (Xu et al., 2021). However, the magnitudes of k_1 and k_2 are in practice constrained by the capacity of the magnetic actuation systems (e.g., the electromagnetic coil system described in SI section S4A). Therefore, the magnetic actuating signals in Eq. (S2.14) are computed based

on the highest permissible magnitudes of k_1 and k_2 . Once the values of k_1 and k_2 are determined, these actuating signals will be specified according to the global reference frame via this mapping:

$$\begin{pmatrix} \vec{B}_{\{G\}} \\ \vec{B}_{grad,\{G\}} \end{pmatrix} = \begin{bmatrix} \mathbf{R}_x(\alpha) \mathbf{R}_y(\beta) & \text{amp}; \mathbf{0}_{3 \times 5} \\ \mathbf{0}_{5 \times 3} & \text{amp}; \mathbf{A}_2(\alpha, \beta) \end{bmatrix} \begin{pmatrix} \vec{B}_{\{I\}} \\ \vec{B}_{grad,\{I\}} \end{pmatrix},$$

where

$$\mathbf{R}_x(\alpha) = \begin{pmatrix} 1 & \text{amp}; 0 & \text{amp}; 0 \\ 0 & \text{amp}; \cos \alpha & \text{amp}; -\sin \alpha \\ 0 & \text{amp}; \sin \alpha & \text{amp}; \cos \alpha \end{pmatrix}, \quad \mathbf{R}_y(\beta) = \begin{pmatrix} \cos \beta & \text{amp}; 0 & \text{amp}; \sin \beta \\ 0 & \text{amp}; 1 & \text{amp}; 0 \\ -\sin \beta & \text{amp}; 0 & \text{amp}; \cos \beta \end{pmatrix},$$

and

$$\mathbf{A}_2(\alpha, \beta) = \begin{bmatrix} \cos(\alpha) \cos(2\beta) & \sin(\alpha) \sin(\beta) & \cos(\alpha) \sin(2\beta) & 0.5 \cos(\alpha) \sin(2\beta) \\ 0.5 \sin(2\alpha) \sin(2\beta) & \cos(2\alpha) \cos(\beta) & -0.5 \sin(2\alpha) \cos(2\beta) & 0.5 \sin(2\alpha) (1 + \sin^2 \alpha) \\ -\cos^2(\alpha) \sin(2\beta) & \text{amp}; \sin(2\alpha) \cos(\beta) & \text{amp}; \cos^2(\alpha) \cos(2\beta) & \text{amp}; \sin^2(\alpha) - \cos^2(\alpha) \sin(2\beta) \\ -\sin^2(\alpha) \sin(2\beta) & -\sin(2\alpha) \cos(\beta) & \sin^2(\alpha) \cos(2\beta) & \cos^2(\alpha) - \sin^2(\alpha) \sin(2\beta) \\ -\sin(\alpha) \cos(2\beta) & \cos(\alpha) \sin(\beta) & -\sin(\alpha) \sin(2\beta) & -0.5 \sin(\alpha) \sin(2\beta) \end{bmatrix}$$

Equation (S2.15) concludes our proposed six-DOF control as it shows how we can specify the required actuating signals (based on the global reference frame) such that the MMR's desired orientation can become a minimum potential energy configuration. Based on this actuation method, our MMRs can also be controlled to follow a given angular trajectory. This can be done by discretizing the trajectory into a sequence of angular displacements and sequentially make all these orientations into a minimum potential energy configuration. As these actuators have full six-DOF motions, desired magnetic forces can also be applied on the MMRs at any point along the angular trajectory.

C. Additional discussion

Based on the endowed $\vec{M}_{\{M\}}$, the proposed MMR has two unique features which allow it to concurrently achieve six-DOF and multimodal soft-bodied locomotion.

Although the MMR's $|\vec{m}|$ will change according to the strength of \vec{B} (due to having different amounts of deformation), its \vec{m} will always be aligned to \vec{B} for all the 'U'- and inverted 'V'-shaped deformed configurations.

While the value of d_3 in Eq. (S2.9) will change when the proposed MMR undergoes different amounts of deformations, its value will always remain negative across all the deformed configurations of this actuator.

Having these features is highly advantageous because they ensure that the direction of the null spaces in Eq. (S2.14) will remain the same across all the deformed configurations of our proposed MMR. Thus, the general solution of Eq. (S2.14) will be applicable for implementing six-DOF control on our proposed MMR at all times. An important criterion to compute the general solution of Eq. (S2.14) correctly is that the changes in the MMR's \vec{m} and d_1 - d_3 robotic parameters have been fully accounted for when the actuator deforms. For instance, by using the theoretical model in SI section S2A, we are able to predict the deformation of the MMR (γ) well. Using the computed γ , the deformed MMR's $\vec{m}_{\{L\}}$ can be continuously updated by using the following equation: $\vec{m}_{\{L\}} = \iiint \mathbf{R}_x(\gamma) \vec{M}_{\{M\}} dV$. It is important to update the MMR's $\vec{m}_{\{L\}}$ so that the pseudo-inverse solution in Eq. (S2.14) can be computed accurately. In SI section S3, we will elaborate

how the d_1 - d_3 robotic parameters of our MMR will vary as the actuator undergoes different amounts of deformation.

Equation (S2.14) suggests that the magnitude of the second null space vector will approach infinity when $\theta = \pm \frac{\pi}{4}$. Those angles of θ are known as the singularity angles (4). The values of the singularity angles, however, can be altered via changing the format of the second null space vector:

$$\begin{pmatrix} \vec{B}_{\{I\}} \\ \vec{B}_{grad,\{I\}} \end{pmatrix} = \mathbf{C}^T [\mathbf{C}\mathbf{C}^T]^{-1} \begin{pmatrix} \vec{0}_{3 \times 1,\{I\}} \\ \vec{F}_{desired,\{I\}} \end{pmatrix} + k_1 \begin{pmatrix} 0 \\ 0 \\ 1 \\ 0 \\ 0 \\ 0 \\ 0 \\ 0 \end{pmatrix}_{\{I\}} + k_2 \begin{pmatrix} 0 \\ 0 \\ 0 \\ 0 \\ 0 \\ 0 \\ -\cot(2\theta) \\ 1 \end{pmatrix}_{\{I\}}. \quad (S2.16)$$

By alternating the format of the second null space vector according to the range of θ , the singularity issues can be moderated because the MMR will be able to avoid all the singularity points as it undergoes an angular trajectory.

Section S3- Analysis of sixth-DOF torque

This section presents the numerical analysis for computing the producible sixth-DOF torque of our MMR. In addition, we also compare this torque to the producible sixth-DOF torque of existing MMRs that have single-wavelength, harmonic magnetization profiles (Hu et al., 2018; Ren et al., 2021; Demir et al., 2021; Culha et al., 2020; Diller et al., 2014; Zhang & Diller, 2018; Zhang & Diller, 2015; Zhang et al., 2016). We will also discuss how the other robotic parameters of our MMR will vary as the actuator undergoes different amounts of deformation.

Based on our derivations in SI section S2B, the sixth-DOF torque of our MMR can be determined by analyzing the third row of Eq. (S2.8). Specifically, the sixth-DOF torque of the MMR, $T_{z,\{L\}}$, can be expressed mathematically according to its local reference frame as:

$$T_{z,\{L\}} = d_3 \frac{\partial B_{y,\{L\}}}{\partial x_{\{L\}}}. \quad (S3.1)$$

According to Eq. (S3.1), the sixth-DOF torque of our MMR can be enhanced by either increasing the magnitudes of $|d_3|$ or $\frac{\partial B_{y,\{L\}}}{\partial x_{\{L\}}}$. Since the magnitude of $\frac{\partial B_{y,\{L\}}}{\partial x_{\{L\}}}$ is dependent on the capacity of the magnetic actuation systems (e.g., the electromagnetic coil system described in SI section S4A), it is therefore ideal for the MMR to maximize its $|d_3|$ so that $T_{z,\{L\}}$ can be optimized. From the physical perspective, the magnitude of $|d_3|$ represents the normalized sixth-DOF torque of the MMR, i.e., the producible sixth-DOF torque of the MMR after it has been normalized according to the strength of the actuating signals. It is noteworthy that MMRs with larger $|d_3|$ will be able to produce larger sixth-DOF torque across all types of magnetic actuation systems (Xu et al., 2021).

As d_3 is dependent on the magnetization profile and geometries of the MMR (Eq. (S2.9)), $|d_3|$ will vary as the actuator undergoes different amounts of deformation. Using Eq.s (S2.7) and (S2.9), we can compute $|d_3|$ of our MMR across all possible ‘U’- and inverted ‘V’-shaped deformation configurations that can be generated by our magnetic actuation system (Fig. S6B), i.e., by adjusting $B_{z,\{L\}}$ from -30 mT to 30 mT. For these

simulations, Eq.s (S2.7) and (S2.9) are solved by using the MMR geometries shown in Fig. S1 as well as the following material properties that have been obtained via experimental means (SI section S1B): $|\vec{M}_{\{M\}}| = 9.40 \times 10^4 \text{ A m}^{-1}$ and $E = 271 \text{ kPa}$. Based on these simulations, we can conclude that while $|d_3|$ is non-zero across all the deformation configurations of our proposed MMR, it will be favorable for $B_{z,\{L\}}$ to be applied within 4-6 mT so that our actuator can maximize its $|d_3|$ (Fig. S6B). In general, the information in Fig. S6B is critical in our six-DOF control strategy because it allows us to determine the required $\frac{\partial B_{y,\{L\}}}{\partial x_{\{L\}}}$ that can generate the desired sixth-DOF torque for the proposed MMR. The information in Fig. S6B is also important for computing the pseudo-inverse solution in Eq. (S2.14). Based on the simulation results in Fig. S6B, the predicted $|d_3|$ value of our MMR is computed as $1.02 \times 10^{-7} \text{ N m}^2 \text{ T}^{-1}$ when the actuator is undeformed, i.e., when $B_{z,\{L\}} = 0$. We have compared this predicted value to our MMR's normalized sixth-DOF torque obtained via the experiments illustrated in Fig. 2. The simulation results from Fig. S6B also suggest that the MMR may produce higher normalized sixth-DOF torque if it does not remain perfectly in its undeformed configuration.

The key difference between our proposed MMR and other existing similar MMRs with harmonic magnetization profile (Hu et al., 2018; Ren et al., 2021; Demir et al., 2021; Culha et al., 2020; Diller et al., 2014; Zhang & Diller, 2018; Zhang & Diller, 2015; Zhang et al., 2016) is that our phase shift angle (φ) is different. Here we report that having different φ in the harmonic magnetization profile will significantly affect the MMR's achievable $|d_3|$. To investigate the relationship between φ and $|d_3|$, numerical simulations based on Eq.s (S2.7) and (S2.9) have been conducted. In these simulations, we assume that all the MMRs have the geometries shown in Fig. S1 and their material properties are equal to those of our proposed MMR (SI section S1B): $|\vec{M}_{\{M\}}| = 9.40 \times 10^4 \text{ A m}^{-1}$ and $E = 271 \text{ kPa}$. The magnetization profile of an MMR with a generic φ , $\vec{M}_{\varphi,\{M\}}(s)$, can be mathematically expressed in the simulations as:

$$\vec{M}_{\varphi,\{M\}}(s) = \left| \vec{M}_{\{M\}}(s) \right| \left(0, \quad \text{amp}; \cos\left(-\frac{2\pi}{L}s + \varphi\right), \quad \text{amp}; \sin\left(-\frac{2\pi}{L}s + \varphi\right) \right)^T. \quad (\text{S3.2})$$

In the simulations, we also assume that all the MMRs have a harmonic magnetization profile that has a single wavelength because only such harmonic profiles have so far allowed MMRs to achieve multimodal soft-bodied locomotion (Hu et al., 2018; Ren et al., 2021). The results from our simulation are presented in Fig. S6A, where we plotted the highest achievable $|d_3|$ of the MMRs, $|d_{3,highest}|$, against different φ . From these results, it can be seen that the maximum $|d_{3,highest}|$ will be achieved when $\varphi = \pm 90^\circ$. Hence, we have selected $\varphi = -90^\circ$ for our proposed MMR so that its producible sixth-DOF torque can be maximized. In comparison to existing MMRs with harmonic magnetization profiles that have φ of 45° (Hu et al., 2018; Ren et al., 2021; Demir et al., 2021; Culha et al., 2020) and 0° (Diller et al., 2014; Zhang & Diller, 2018; Zhang & Diller, 2015; Zhang et al., 2016), the simulation results in Fig. S6A indicate that our proposed MMR can produce 1.40-76.0 folds larger $|d_{3,highest}|$ than such existing actuators. Because the achievable $|d_3|$ of the MMRs will change as the actuators deform, we have also used Eq.s (S2.7) and (S2.9) to compute how $|d_3|$ will vary with $B_{z,\{L\}}$ for existing MMRs that have a harmonic magnetization profile with φ of 45° (Hu et al., 2018; Ren et al., 2021; Demir et al., 2021; Culha et al., 2020) and 0° (Diller et al., 2014; Zhang & Diller, 2018; Zhang & Diller, 2015; Zhang et al., 2016) (Fig. S6B). These simulation results indicate that the average $|d_3|$ of our proposed MMR ($5.77 \times 10^{-8} \text{ A m}^3$) is 1.41-63.9 folds larger than those that have φ of 45° ($4.10 \times 10^{-8} \text{ A m}^3$) (Hu et al., 2018; Ren et al., 2021; Demir et al., 2021; Culha et al., 2020) and 0° ($9.03 \times 10^{-10} \text{ A m}^3$) (Diller et al., 2014; Zhang & Diller, 2018; Zhang & Diller, 2015; Zhang et al., 2016). Note that the average $|d_3|$ of these MMRs is computed via the following integral: $\frac{\int_{-30}^{30} |d_3| dB_{z,\{L\}}}{60}$, i.e., finding their corresponding area under the curve in Fig. S6B and subsequently dividing those areas across the entire domain of $B_{z,\{L\}}$. The numerical simulations in Fig. S6B therefore suggest that the proposed MMR is able to produce much higher sixth-DOF torques than existing similar actuators that have φ of 45° (Hu et al.,

2018; Ren et al., 2021; Demir et al., 2021; Culha et al., 2020) and 0° (Diller et al., 2014; Zhang & Diller, 2018; Zhang & Diller, 2015; Zhang et al., 2016).

A notable advantage of our proposed MMR is that its sixth-DOF torque has been optimized without compromising its actuation capabilities in the traditional five-DOF motions. This is because the achievable net magnetic moment of our proposed MMR has the same magnitude with all other MMRS that have single-wavelength, harmonic magnetization profiles (Hu et al., 2018; Ren et al., 2021; Demir et al., 2021; Culha et al., 2020; Diller et al., 2014; Zhang & Diller, 2018; Zhang & Diller, 2015; Zhang et al., 2016). To prove this hypothesis mathematically, we first reanalyze the generic magnetization profile in Eq. (S3.2) and arrange it to the following format:

$$\begin{aligned}\vec{M}_{\varphi, \{M\}}(s) &= \mathbf{R}_x(\varphi) \left| \vec{M}_{\{M\}}(s) \right| \left(0, \text{ amp}; \cos\left(-\frac{2\pi}{L}s\right), \text{ amp}; \sin\left(-\frac{2\pi}{L}s\right) \right)^T \\ &= \mathbf{R}_x(\varphi) \vec{M}_{\varphi 0, \{M\}}(s),\end{aligned}$$

where

$$\vec{M}_{\varphi 0, \{M\}}(s) = \left| \vec{M}_{\{M\}}(s) \right| \left(0, \text{ amp}; \cos\left(-\frac{2\pi}{L}s\right), \text{ amp}; \sin\left(-\frac{2\pi}{L}s\right) \right)^T, \quad (\text{S3.3})$$

and it represents the harmonic magnetization profile of an MMR that has a φ value of 0° . When an MMR with a generic φ undergoes a spatially varying rotary deformation, $\gamma(s)$, across its body, it can possess the following net magnetic moment (\vec{m}_{φ}):

$$\vec{m}_{\varphi} = \iiint \mathbf{R}_x(\gamma) \vec{M}_{\varphi, \{M\}} dV = \iiint \mathbf{R}_x(\gamma) \mathbf{R}_x(\varphi) \vec{M}_{\varphi 0, \{M\}} dV. \quad (\text{S3.4})$$

A unique characteristics of MMRs with harmonic magnetization profile is that, regardless of φ , they will always be able to produce the same amount of deformation, $\gamma(s)$, under the same $B_{z, \{L\}}$ (Hu et al., 2018). This is assuming that the $z_{\{L\}}$ -axis of the MMR is always assigned to be parallel to the actuators' net magnetic moment (\vec{m}_{φ}) (Hu et al., 2018). Due to this unique feature, our analysis in Eq. (S3.4) can therefore be simplified because we do not need to account for different deformation characteristics, $\mathbf{R}_x(\gamma)$, for MMRs with different φ .

Because $\mathbf{R}_x(\varphi)$ is constant across the entire MMR, Eq. (S3.4) can be rearranged into the following format:

$$\vec{m}_{\varphi} = \iiint \mathbf{R}_x(\gamma) \mathbf{R}_x(\varphi) \vec{M}_{\varphi 0, \{M\}} dV$$

$$\begin{aligned}
 &= \iiint \mathbf{R}_x(\varphi) \mathbf{R}_x(\gamma) \vec{M}_{\varphi 0, \{M\}} dV \\
 &= \mathbf{R}_x(\varphi) \iiint \mathbf{R}_x(\gamma) \vec{M}_{\varphi 0, \{M\}} dV \\
 &= \mathbf{R}_x(\varphi) \vec{m}_{\varphi 0},
 \end{aligned}$$

where

$$\vec{m}_{\varphi 0} = \iiint \mathbf{R}_x(\gamma) \vec{M}_{\varphi 0, \{M\}} dV, \quad (S3.5)$$

and it represents the net magnetic moment produced by a deformed MMR that has a magnetization profile of $\vec{M}_{\varphi 0, \{M\}}(s)$. Since the rotational matrix, $\mathbf{R}_x(\varphi)$, is an orthonormal matrix, Eq. (S3.5) concludes that the magnitude of \vec{m}_{φ} is equal to $\vec{m}_{\varphi 0}$ for all values of φ , including our proposed \vec{M} that has a φ value of -90° . As a result, this implies that our proposed MMR does possess a \vec{m} that has the same magnitude with all other MMRS that have single-wavelength, harmonic magnetization profiles (Hu et al., 2018; Ren et al., 2021; Demir et al., 2021; Culha et al., 2020; Diller et al., 2014; Zhang & Diller, 2018; Zhang & Diller, 2015; Zhang et al., 2016). Therefore, our proposed MMR is able to maximize its sixth-DOF torque without compromising its actuation capabilities for the traditional five-DOF motions.

To successfully implement six-DOF control on our proposed MMR, we have also analyzed how its d_1 and d_2 robotic parameters in the \mathbf{D} matrix of Eq. (S2.9) will vary as it undergoes different amounts of deformation. These simulation results can be found in Fig. S7. While the values of d_1 and d_2 do not affect the producible sixth-DOF torque of our MMR, it is still important to model these parameters so as to compute the pseudo-inverse solution in Eq. (S2.14) accurately.

Section S4- Experiments

In this section, we would describe our magnetic actuation system in section S4A. Subsequently, we would elaborate on the experiments that evaluated the producible sixth-DOF torque of the proposed MMR (section S4B). We would also include additional discussion pertaining to the rolling (section S4C) and jellyfish-like swimming locomotion (section S4D). Finally, we would conclude this section by discussing the undulating swimming and meniscus-climbing locomotion of our MMR in section S4E.

A. Magnetic actuation system

Our magnetic actuation system was a customized electromagnetic coil system, which had a nine-coil configuration (Fig. S8). For all the experiments, the proposed MMR was placed at the center of the coil system, which had a workspace of $16 \text{ mm} \times 16 \text{ mm} \times 16 \text{ mm}$ that could produce a 90% homogeneous field. By controlling the electrical current in the coils, we could generate the desired actuating magnetic signals for our proposed MMR. This system could produce a maximum $|\vec{B}|$ of 30 mT, and the highest producible spatial gradient of the coil system was 0.4 T m^{-1} . The smallest angular change achievable by our applied \vec{B} was 0.57° while the resolution of the field's spatial gradients was 0.01 T/m .

B. Experimental investigation on the MMR's sixth-DOF torque

In the experiment illustrated in Fig. 2, we could deduce the sixth-DOF torque generated by our undeformed MMR via measuring the angular deflection at the free end of the fixed-free beam, θ_{tip} , and subsequently applying the Euler-Bernoulli equation. Based on the Euler-Bernoulli equation, the governing equation for describing the deformation of the larger fixed-free beam could be expressed as (Lum et al., 2016):

$$M_{\text{bt}}(s_{\text{bt}}) = E_{\text{bt}} I_{\text{bt}} \frac{\partial \theta_{\text{bt}}}{\partial s_{\text{bt}}}(s_{\text{bt}}), \quad (\text{S4.1})$$

where M_{bt} and θ_{bt} represented the bending moment and the angular deflections along the length of the fixed-free beam, s_{bt} , respectively (see Fig. S9 for θ_{bt} and s_{bt}). The variable E_{bt} represented the Young's modulus of the fixed-free beam, and this parameter was evaluated to be $787 \pm 8.18 \text{ kPa}$ via a standard compression test (SHIMADZU AG-X plus, 10 kN). The remaining variable, I_{bt} , represented the second moment of area of the fixed-free beam, and it could be computed as $3.90 \times 10^{-15} \text{ m}^4$ based on the beam's dimensions.

In theory, the sixth-DOF torque generated by our magnetic beam, $T_{z,\{L\}}$, would induce a constant M_{bt} across the larger fixed-free beam, and the magnitudes of $T_{z,\{L\}}$ and M_{bt} would be equal. By applying such loading conditions and the fixed-free boundary conditions to Eq. (S4.1), $T_{z,\{L\}}$ could be deduced by the following equation:

$$T_{z,\{L\}} = \frac{E_{\text{bt}} I_{\text{bt}}}{L_{\text{bt}}} \theta_{\text{tip}}, \quad (\text{S4.2})$$

where $L_{\text{bt}} = 16 \times 10^{-3} \text{ m}$ and it represented the total length of the fixed-free beam (Fig. S9). Using Eq. (S4.2), we could therefore execute the experiments in Fig. 2A and establish the relationship between $T_{z,\{L\}}$ and the actuating magnetic signals (Fig. 2B).

C. Rolling locomotion

By having six-DOF, our soft MMR could choose to roll along its length (rotating about the $x_{\{L\}}$ -axis) or along its width (rotating about the $y_{\{L\}}$ -axis). Assuming no-slip conditions, the achievable speed for both types of these rolling locomotion would theoretically be linearly proportional to the frequency of the applied rotating \vec{B} (Hu et al., 2018). To validate this hypothesis, experiments were conducted to establish the relationship between the rolling speed of our MMR with respect to different rotating frequencies of \vec{B} . For the experiments pertaining to rolling along the length of the MMR, the magnitude of \vec{B} was held constant at 15 mT while the frequency of \vec{B} varied between 0.25 Hz to 10 Hz. The data of these experimental results were presented in Fig. S10. In general, the experimental data agreed that there was a linear relationship between the rolling speed of the MMR and the frequency of the applied \vec{B} .

For the experiments pertaining to rolling along the width of the MMR, the magnitude of \vec{B} was held constant at 6 mT so that this actuator could produce a gentler curvature that would be favorable for negotiating across narrow barriers (Fig. S11). The rolling speeds for this type of rolling were measured as the frequency of the rotating \vec{B} was varied from 0.25 Hz to 3 Hz (Fig. S10). In general, the relationship between the rolling speed of the MMR and the frequency of the applied \vec{B} was linear, and therefore the experiments agreed with the theoretical prediction. As predicted by the theory, the speed achievable by rolling along the width of the MMR was slower than the speed of the MMR when it rolled along its length (Fig. S10).

D. Jellyfish-like swimming locomotion

For the jellyfish-like swimming locomotion, the average speeds (V_R) of our MMR were 7.65×10^{-3} m s^{-1} , 10.4×10^{-3} m s^{-1} and 9.49×10^{-3} m s^{-1} when it was rotating about the $x_{\{L\}}$ -, $y_{\{L\}}$ - and $z_{\{L\}}$ -axes, respectively. Therefore, the Reynolds number (Re) in these experiments could be computed as 54.9, 74.6 and 68.1, respectively. Note that $Re = \frac{V_R L_R}{\nu}$, where the length of our MMR, L_R , was 6.4 mm (Fig. S1) and the kinematic viscosity of water at 25°C, ν , was 8.92×10^{-7} m² s⁻¹ (Kestin et al., 1978). In a similar way, the Reynolds number of our MMR could be calculated to be 67.2 when it executed the experiments in SI Video S8 (average swimming speed: 9.37×10^{-3} m s^{-1}).

E. Undulating swimming and meniscus climbing locomotion

On an air-water interface, our soft MMR could swim via an undulating locomotion. This gait could be activated by rotating \vec{B} continuously in the MMR's $y_{\{L\}}z_{\{L\}}$ plane so that a traveling wave could be generated along the soft body of the MMR (Fig. S12A and SI Video S10) (Hu et al., 2018; Diller et al., 2014; Zhang & Diller, 2018; Zhang & Diller, 2015; Zhang et al., 2016). As this is a non-reciprocal swimming gait, our proposed MMR could produce a net propulsion in low Reynolds number regimes ($Re : 3.45$). By controlling the MMR's sixth-DOF angular displacement, we could also steer this actuator to follow an 'L'-shaped trajectory on the air-water interface (Fig. S12B and SI Video S10). Our experiments indicated that the proposed MMR could swim at a speed of 5.80 mm s^{-1} when the applied \vec{B} of strength 20 mT was rotating at a frequency of 10 Hz.

Alternatively, our soft MMR could also choose to climb up the meniscus of an air-water interface. By applying \vec{B} (25 mT) along the $z_{\{L\}}$ -axis of the MMR, we could deform this actuator into its 'U'-shaped configuration (Fig. S12C(i) and (ii)). In this deformed configuration, the MMR could displace more water and generate a greater buoyancy force (Hu et al., 2018). By increasing the buoyancy of the MMR, we could rotate our actuator to perform the meniscus-climbing locomotion (Fig. S12C(ii)-(iv)).

F. 3D pick-and-place operation

Here we will compute the theoretical angular and linear resolutions of our MMR when it was executing the pick-and-place operation. By exploiting the phenomenon in which the MMR's \vec{m} will tend to align with the applied \vec{B} (Diller et al., 2016; Kummer et al., 2010), we can rotate the actuator about its $x_{\{L\}}$ - and $y_{\{L\}}$ -axes via controlling the direction of \vec{B} (SI Section S2B). Since the smallest angular change in \vec{B} is 0.57° (SI Section S4A), this implied that the angular resolution of the MMR about its $x_{\{L\}}$ - and $y_{\{L\}}$ -axes would be 0.57° too. The sixth-DOF angular resolution of the MMR can be computed based on the resolution of the field's spatial gradients. Based on Eq. (S2.14), it can be seen that the MMR's desired sixth-DOF angle, θ , can be controlled via tuning the field's spatial gradients. Because there were no magnetic forces applied to the MMR during the pick-and-place operation, the pseudo-inverse solution in Eq. (S2.14) would be a null vector (SI section S2B). Hence, the eighth row of Eq. (S2.14) can be simplified to establish the relationship between $\frac{\partial B_{x, \{I\}}}{\partial y_{\{I\}}}$ and θ :

$$\frac{\partial B_{x, \{I\}}}{\partial y_{\{I\}}} = -k_2 \tan(2\theta). \quad (S4.3)$$

By differentiating both sides of Eq. (S4.3) with respect to θ , we can establish the following relationship:

$$\frac{\partial B_{x,y\{I\}}}{\partial \theta} = -2k_2 \sec^2(2\theta),$$

$$\text{where } B_{x,y\{I\}} = \frac{\partial B_{x, \{I\}}}{\partial y_{\{I\}}}. \quad (\text{S4.4})$$

Equation (S4.4) can be approximated as:

$$\Delta B_{x,y\{I\}} = -2k_2 \sec^2(2\theta) \Delta\theta, \quad (\text{S4.5})$$

where $\Delta B_{x,y\{I\}}$ and $\Delta\theta$ represent the resolutions of the field's spatial gradient and the MMR's sixth-DOF, respectively. Based on Eq. (S4.3), we can also express k_2 as:

$$k_2 = -\frac{B_{x,y\{I\}}}{\tan(2\theta)}. \quad (\text{S4.6})$$

By substituting Eq. (S4.6) into Eq. (S4.5), Eq. (S4.5) can then be further simplified and rearranged into:

$$\Delta\theta = \frac{\Delta B_{x,y\{I\}}}{4B_{x,y\{I\}}} \sin(4\theta). \quad (\text{S4.7})$$

To evaluate $\Delta\theta$, we substitute the largest and smallest value of $B_{x,y\{I\}}$ and $\Delta B_{x,y\{I\}}$ respectively into Eq. (S4.7) so that the magnitude of $\Delta\theta$ can be minimized (SI Section S4A):

$$\Delta\theta = 6.25 \times 10^{-3} \sin(4\theta). \quad (\text{S4.8})$$

Although Eq. (S4.8) implies that the sixth-DOF angular resolution of the MMR is dependent on θ , here we assign $\sin(4\theta)$ with the highest value of 1 to obtain the coarsest $\Delta\theta$ for simplicity purposes. In this case, the MMR's sixth angular resolution can therefore be computed via Eq. (S4.8) as 6.25×10^{-3} rad or 0.36° .

To compute the translational resolution of the MMR, the shape of the rolling MMR is approximated to be a circle, which has a radius of 0.95 mm (Fig. S14). To identify the best fit circle, we only consider the deformation of the magnetic beam component when $|\vec{B}| = 20$ mT because this is the applied magnetic field during the pick-and-place operations. Assuming no-slip conditions, the translational resolution achievable by our MMR can therefore be computed by the product of its radius and the $y_{\{L\}}$ -axis angular resolution ($9.5 \mu\text{m}$).

Figures

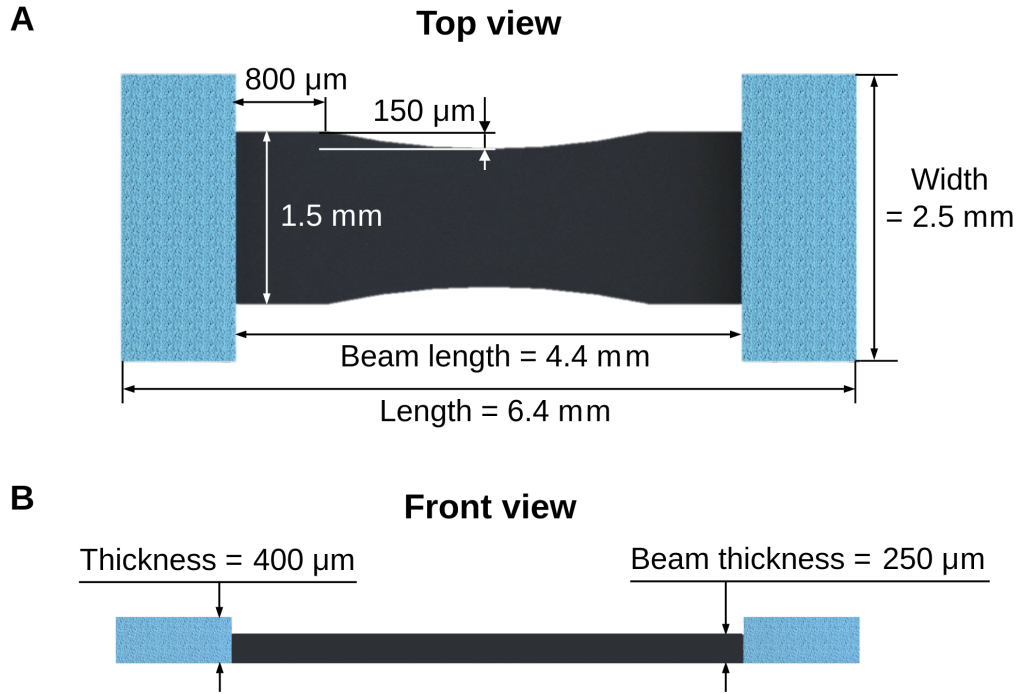


Abbildung 1: Fig. S1. The dimensions of our proposed MMR when it is seen from the (A) top view and (B) front view.

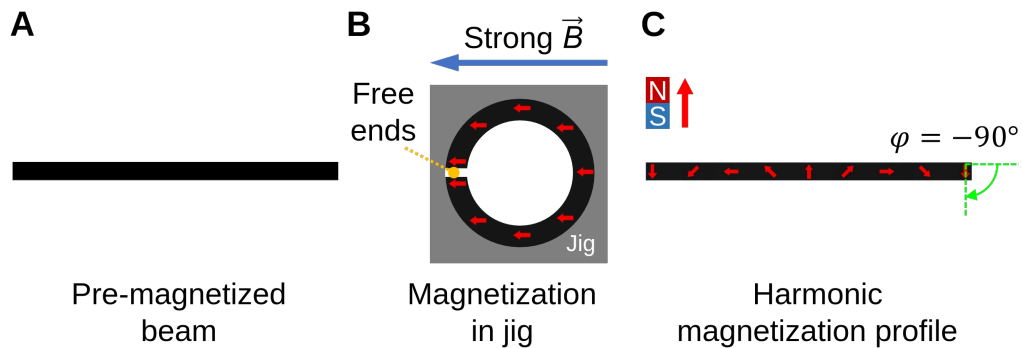


Abbildung 2: Fig. S2. The magnetization process of the magnetic beam component. The pre-magnetized beam in (A) was rolled in a cylindrical jig, and then magnetized by a strong, uniform magnetic field of 1.1 T in (B). The free ends of the beam were illustrated at the exaggerated gap in (B). (C) Once the magnetic beam recovered back to its original shape, it would possess the optimal harmonic magnetization profile that had a phase shift angle (φ) of -90° .

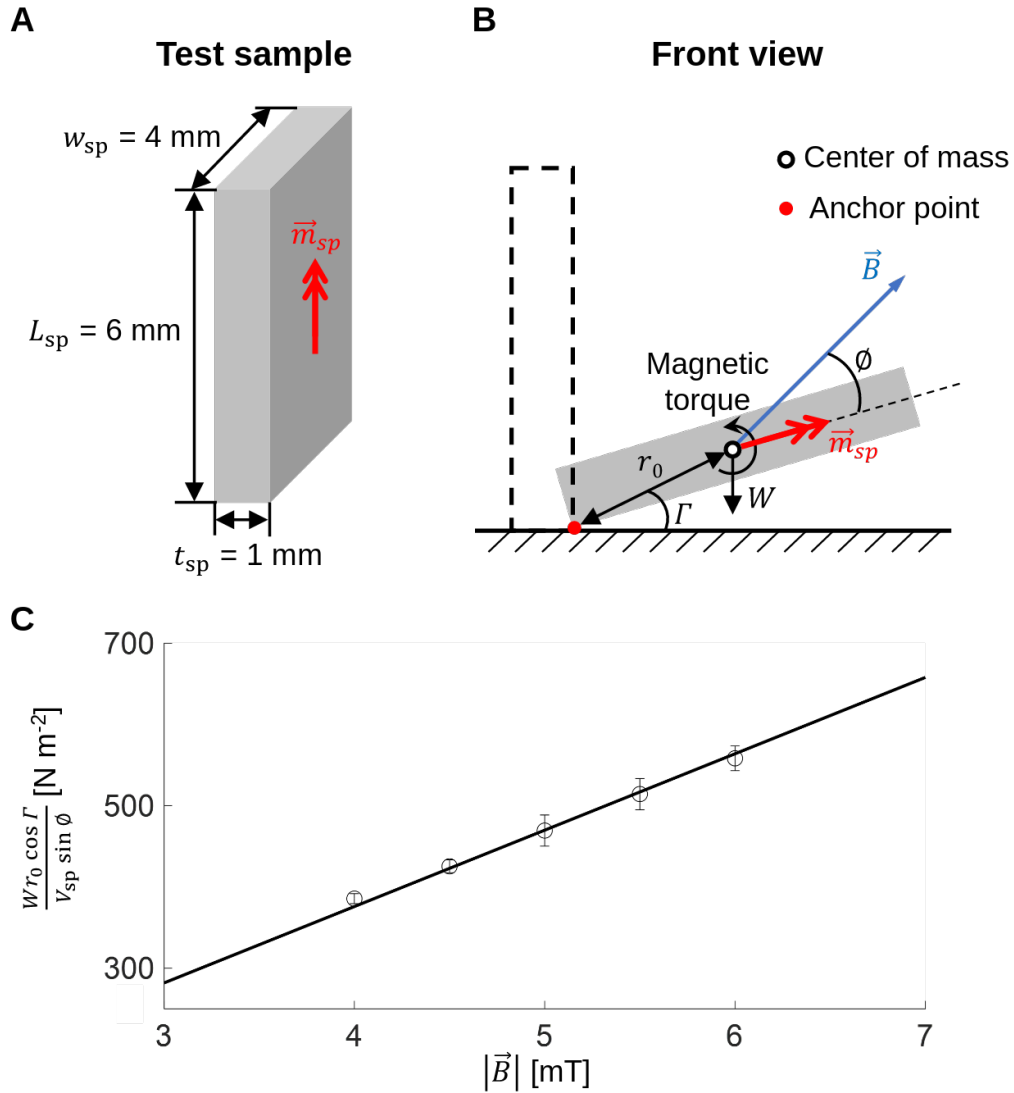


Abbildung 3: Fig. S3. An experiment for evaluating the achievable $|\vec{M}|$ of the proposed MMR. (A) The dimensions and net magnetic moment, \vec{m}_{sp} , of the molded cuboid samples. (B) A free-body diagram analysis for this experiment. (C) The deduced $\frac{W r_0 \cos \Gamma}{V_{sp} \sin \varnothing}$ was plotted against the magnitude of the applied magnetic fields ($|\vec{B}|$). Each data point had five trials and the error bars of the data points represented the standard deviation of these points. The best fit line of this graph was constrained to intersect the origin, and its gradient represented the MMR's achievable $|\vec{M}|$. The gradient of this best fit line was computed to be $9.40 \times 10^4 \text{ A m}^{-1}$.

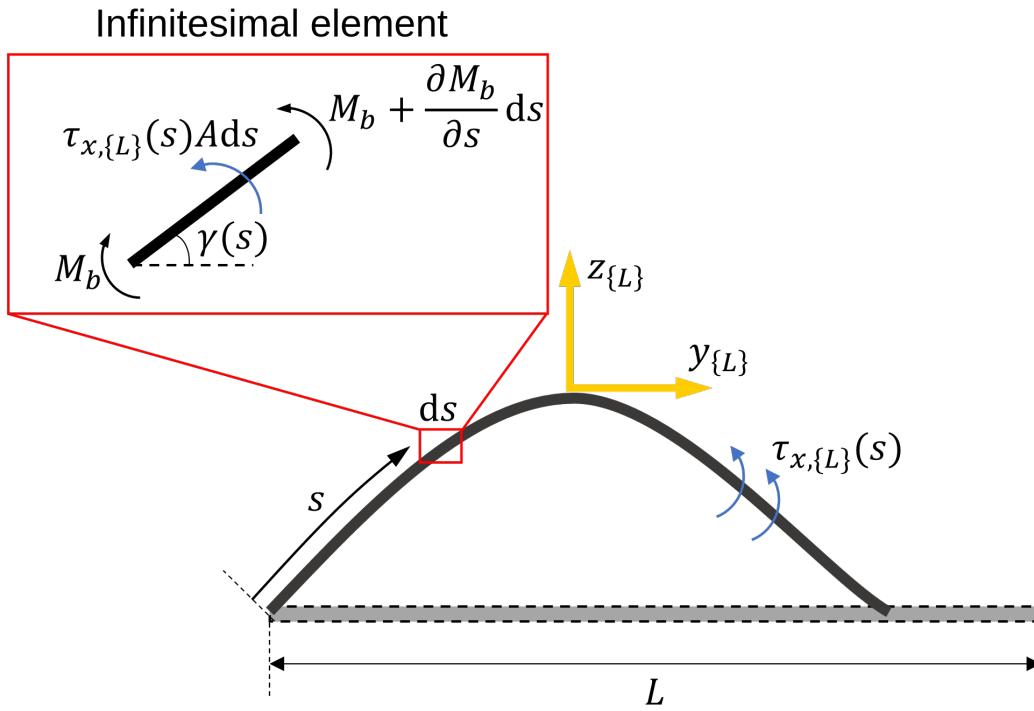


Abbildung 4: Fig. S4. Quasi-static analysis of the magnetic soft beam. The variable, $\tau_{x,\{L\}}(s)$, represents the generated magnetic torque (per unit volume), which is distributed along the entire beam. We only show a segment of $\tau_{x,\{L\}}(s)$ for illustration purposes.

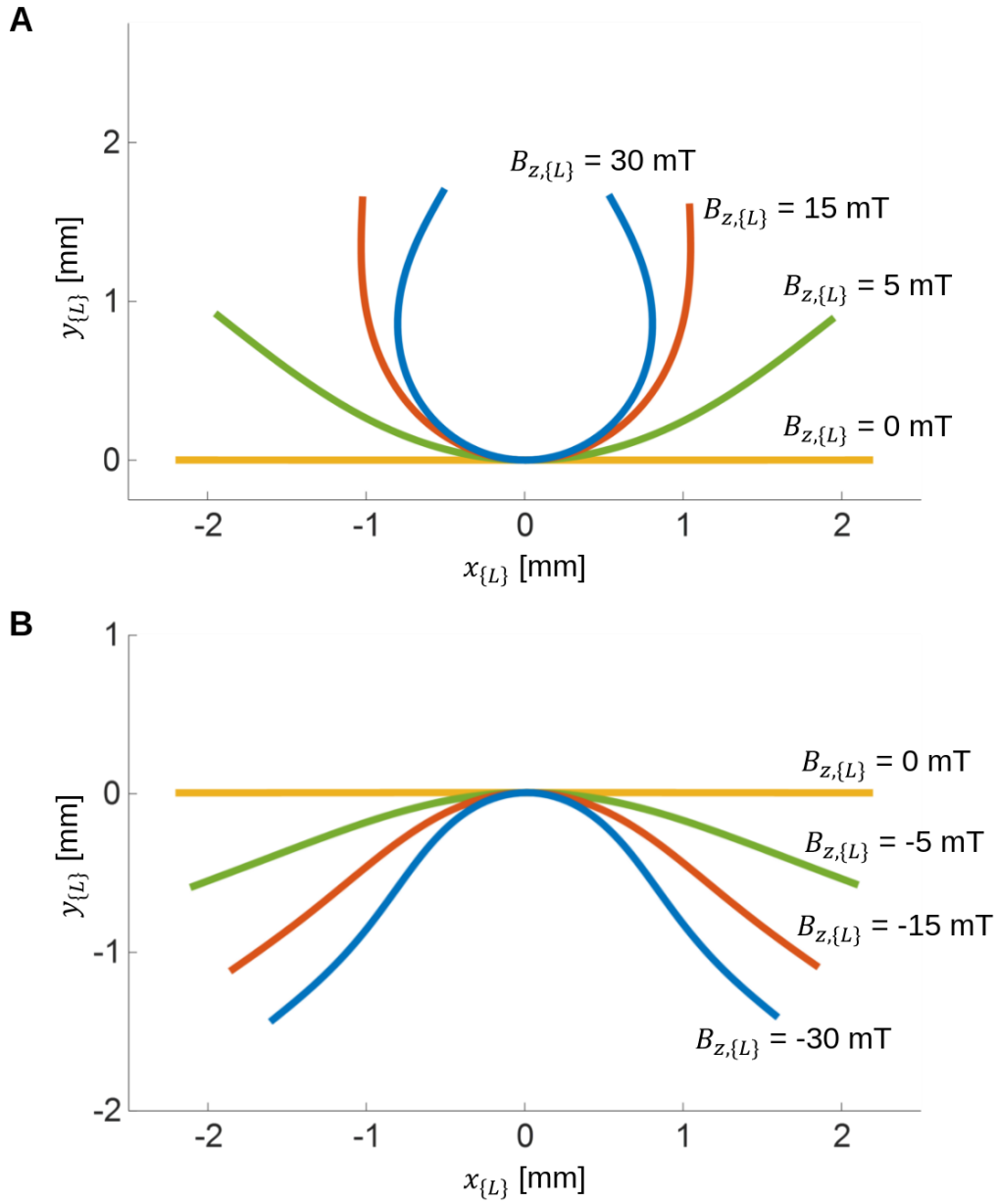


Abbildung 5: Fig. S5. Simulation results of the magnetic beam's deformation when it is subjected to a series of $B_{z,\{L\}}$. As the magnitudes of $B_{z,\{L\}}$ increase, it can be seen that the curvatures of the magnetic beam will become sharper for both the (A) 'U'- and (B) inverted 'V'-shaped configurations.

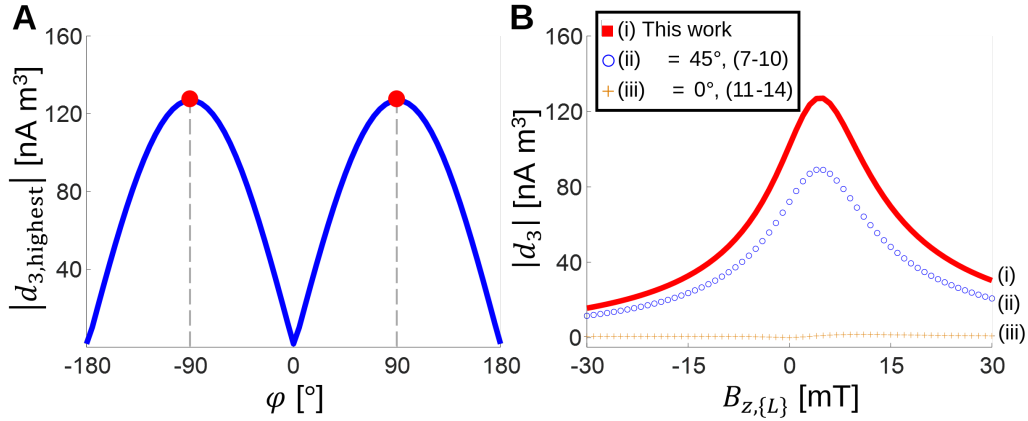


Abbildung 6: Fig. S6. Numerical analysis for the normalized sixth-DOF torque, $|d_3|$, of MMRs with different φ . (A) Plotting the MMRs' $|d_{3,\text{highest}}|$ with respect to different φ , whereby $|d_{3,\text{highest}}|$ is seen to be maximized when $\varphi = \pm 90^\circ$ (indicated by the red dots). From the graph, the $|d_{3,\text{highest}}|$ of our MMR is $1.27 \times 10^{-7} \text{ A m}^3$. For existing MMRs with a harmonic magnetization profile that have φ of 45° (Hu et al., 2018; Ren et al., 2021; Demir et al., 2021; Culha et al., 2020) and 0° (Diller et al., 2014; Zhang & Diller, 2018; Zhang & Diller, 2015; Zhang et al., 2016), their computed $|d_{3,\text{highest}}|$ are $9.06 \times 10^{-8} \text{ A m}^3$ and $1.67 \times 10^{-9} \text{ A m}^3$, respectively. (B) Evaluating the MMRs' $|d_3|$ when they deform under different $B_{z,\{L\}}$. Three different MMRs have been analyzed: (i) our proposed MMR, and existing MMRs with a harmonic magnetization profile that have φ of (ii) 45° (Hu et al., 2018; Ren et al., 2021; Demir et al., 2021; Culha et al., 2020) and (iii) 0° (Diller et al., 2014; Zhang & Diller, 2018; Zhang & Diller, 2015; Zhang et al., 2016). The average $|d_3|$ of each MMR can be computed by finding their corresponding area under the curve and subsequently dividing those areas across the entire domain of $B_{z,\{L\}}$.

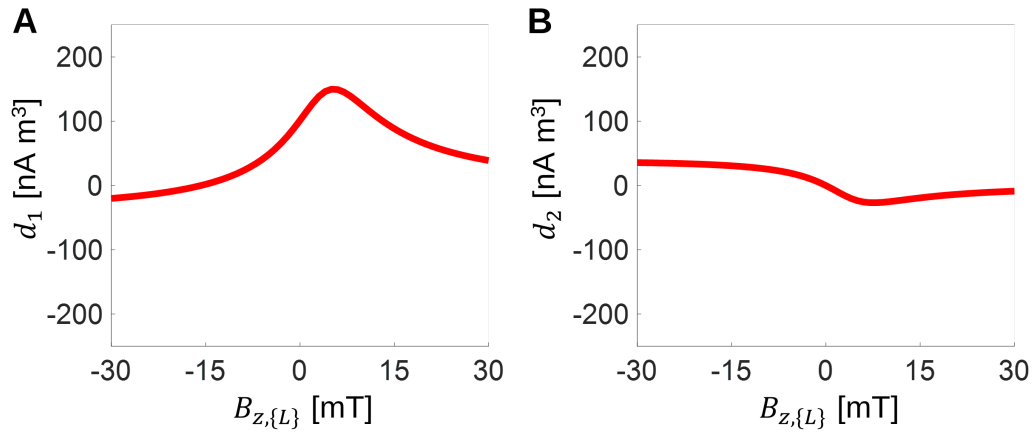


Abbildung 7: Fig. S7. Simulation results of (A) d_1 and (B) d_2 against different $B_{z,\{L\}}$.

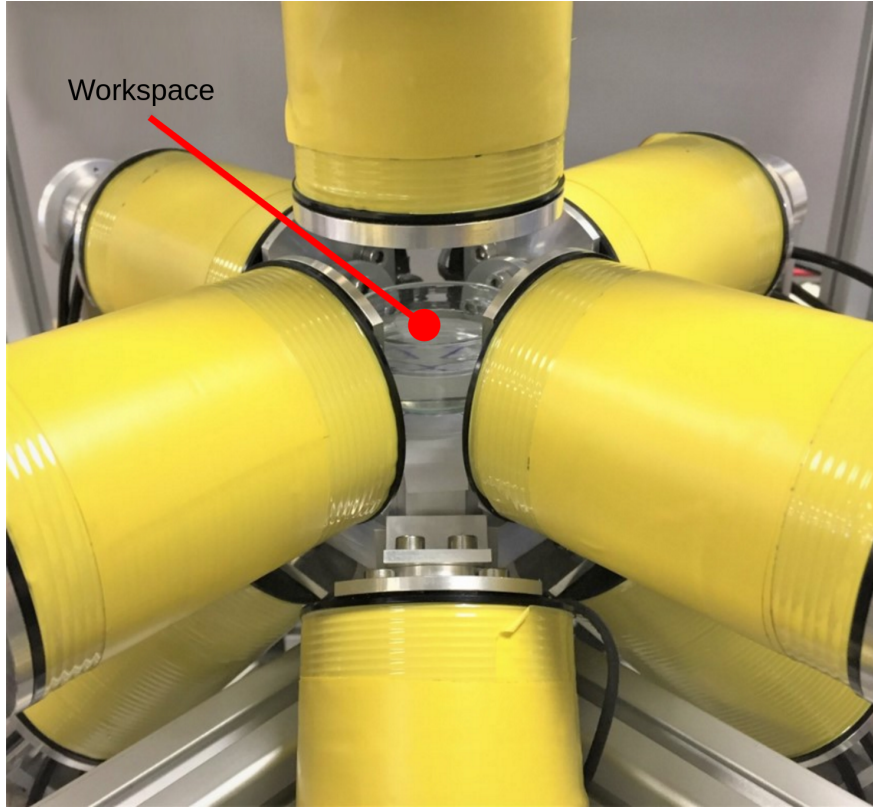


Abbildung 8: Fig. S8. Our customized electromagnetic coil system in which the central workspace of the system was highlighted.

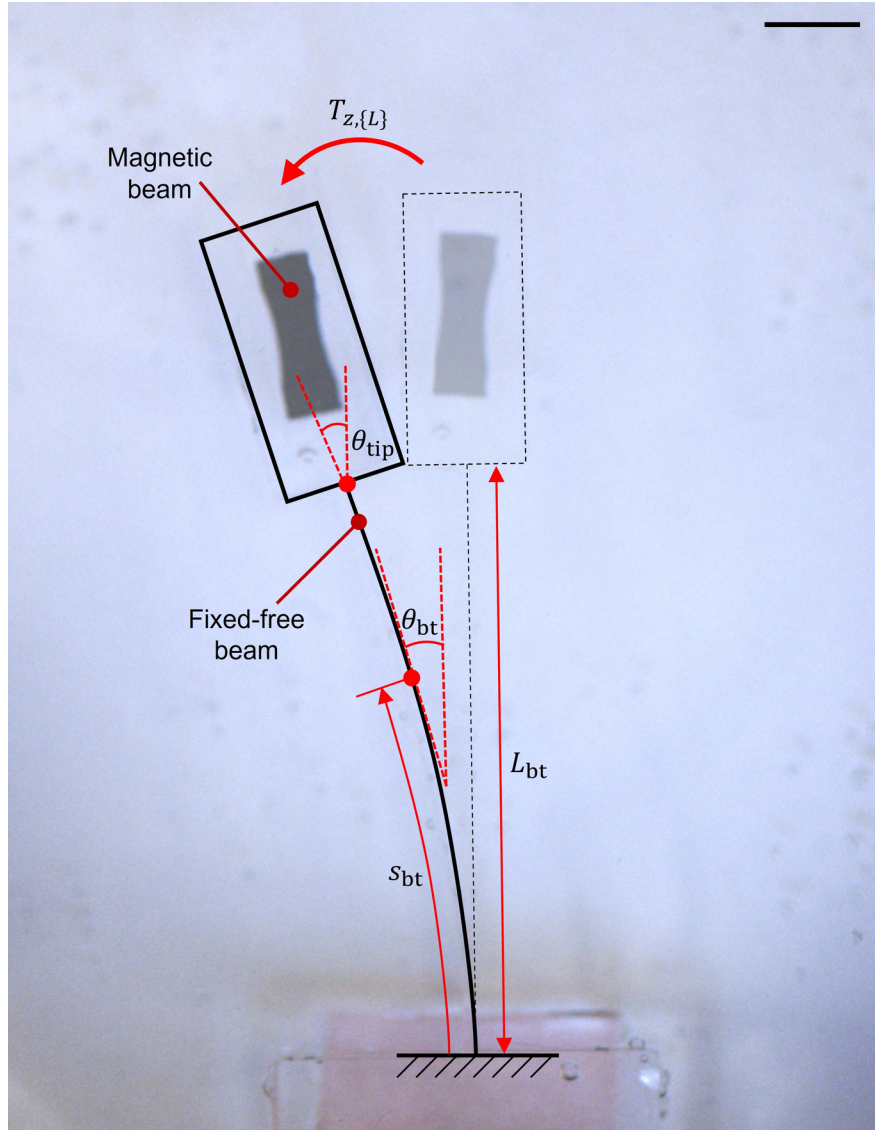


Abbildung 9: Fig. S9. The variables required to deduce the MMR's producible sixth-DOF torque in the experiment shown in Fig. 2 of the main text. Scale bar: 2 mm.

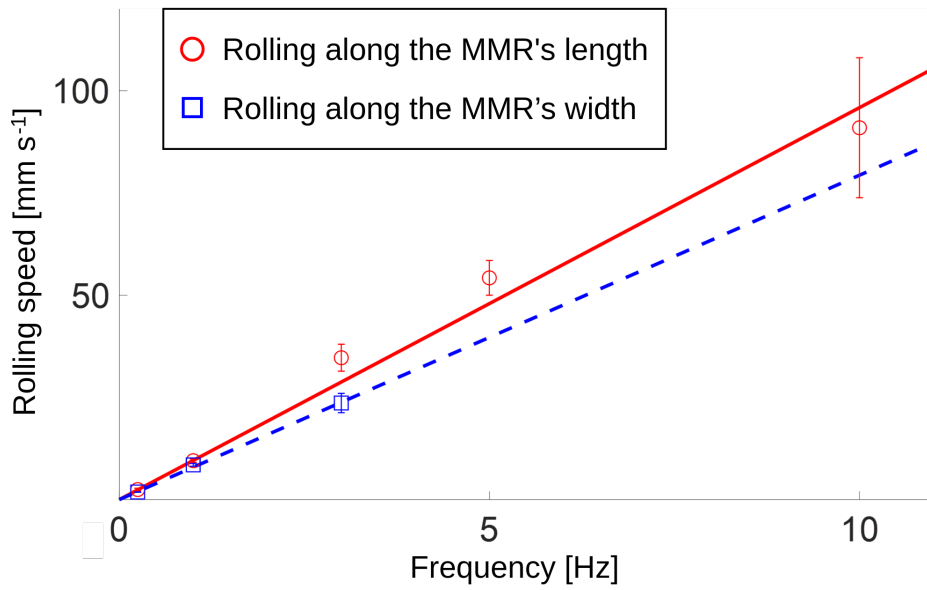


Abbildung 10: Fig. S10. The measured rolling speed plotted against different rotating frequencies of \vec{B} . Each data point had five trials and the error bars represented their corresponding standard deviation. The solid red line and dashed blue line represented the best fit line for the data points pertaining to rolling along the MMR's length and width, respectively. Because higher speed could be achieved when the MMR was rolling along its length than rolling along its width, the gradient of the solid red line was steeper than its dashed blue line counterpart.

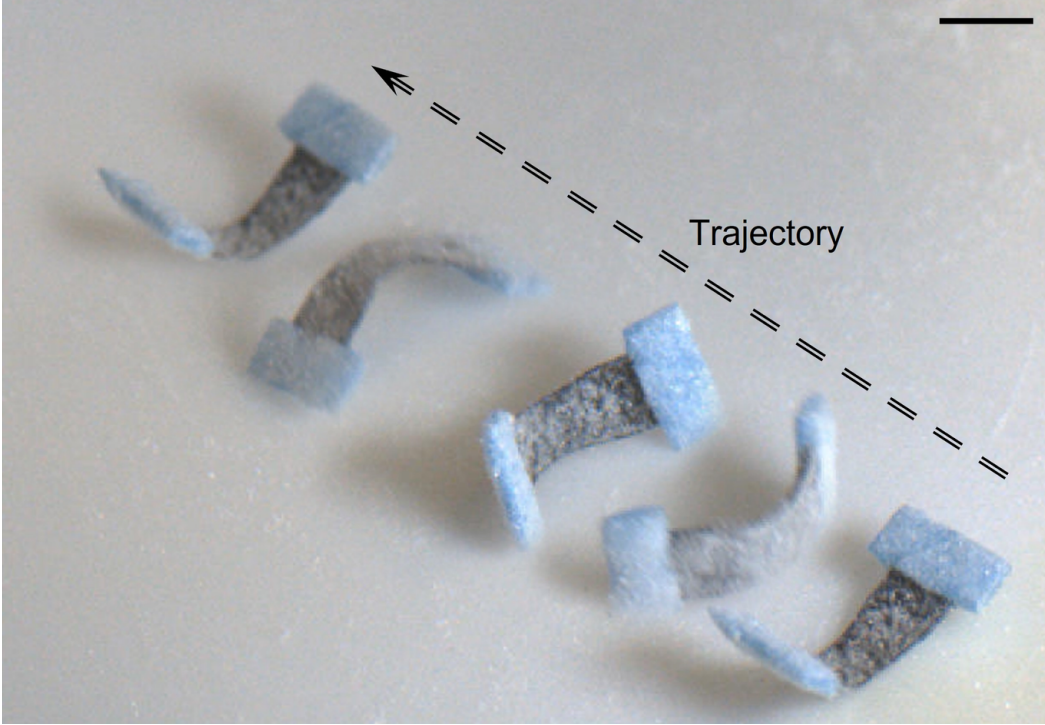


Abbildung 11: Fig. S11. Rolling along the MMR's width with a gentle curvature ($|\vec{B}|=6$ mT). Scale bar: 2 mm.

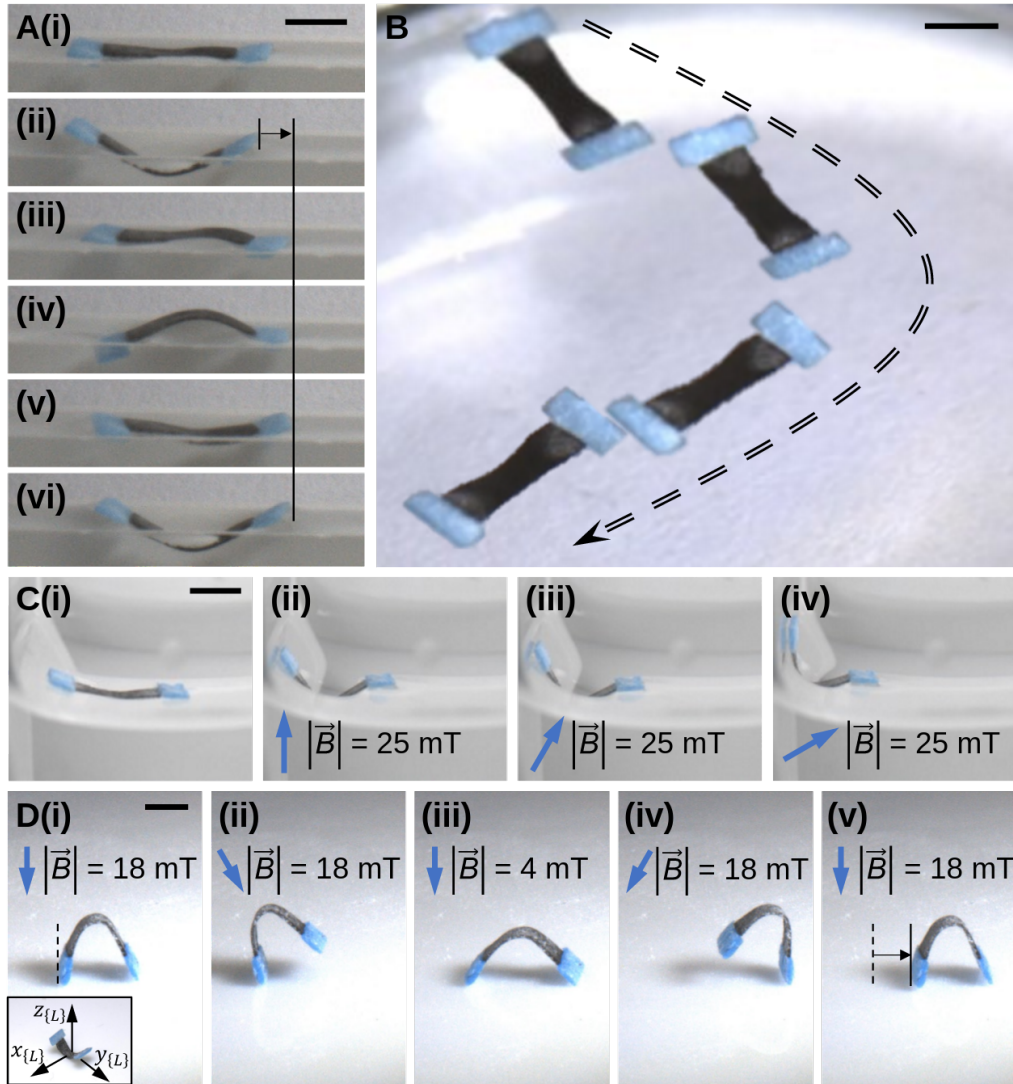


Abbildung 12: Fig. S12. The undulating swimming, meniscus climbing and two-anchor crawling locomotion of the proposed MMR. (A) The MMR could execute its undulating swimming locomotion by continuously generating a traveling wave along its body. (ii)-(vi) The MMR produced a net displacement after generating one period of the traveling wave. (B) As the MMR swam via the undulating swimming locomotion, we could steer it to follow an ‘L’-shaped trajectory. (C) Meniscus-climbing could be executed by the MMR when (i)-(ii) a strong upward \vec{B} ($|\vec{B}|=25$ mT) was applied to deform the actuator and subsequently rotating \vec{B} from (iii) 30° to (iv) 60° (with respect to the vertical upright direction). (D) An illustration of the MMR’s two-anchor crawling locomotion. The dashed line represented the initial location of the MMR’s rear end, and the solid line represented the final location of the MMR’s rear end after it performed one cycle of two-anchor crawling. The distance between the dashed and solid lines represented the net displacement produced by the MMR in one cycle. Scale bars: 2 mm.

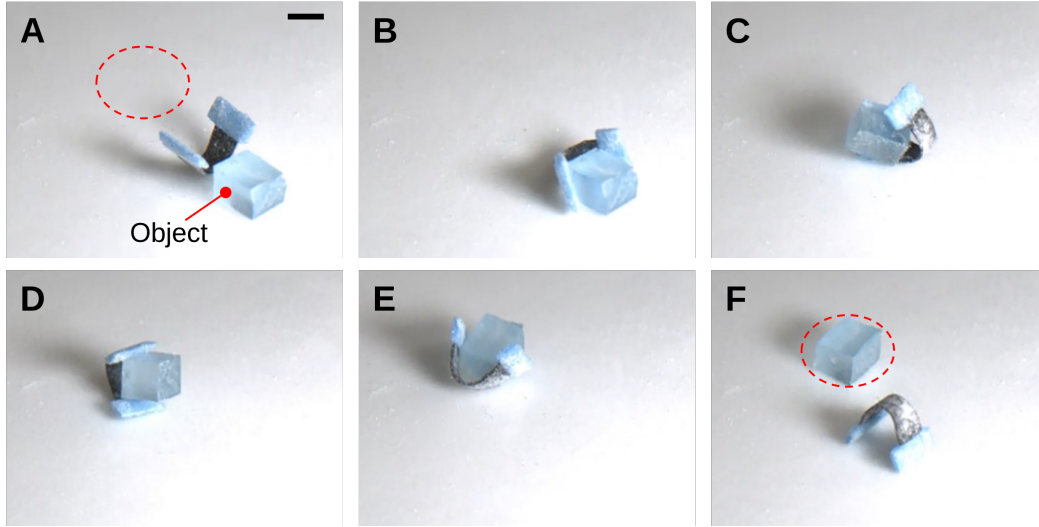


Abbildung 13: Fig. S13. Experiment for evaluating the payload of our soft MMR. As an example, here we presented the experiment procedure of the MMR carrying an object with 3 folds of its weight. The procedures for carrying objects with other weights were the same. (A) The experiment would require the MMR to grab, transport and place the object to the desired placement location (highlighted by the dotted red ellipse). (B) The MMR grabbed the object. (C)-(D) The MMR held on to the object and transported it. (E)-(F) The MMR released the object at the desired placement location. Scale bar: 2 mm.

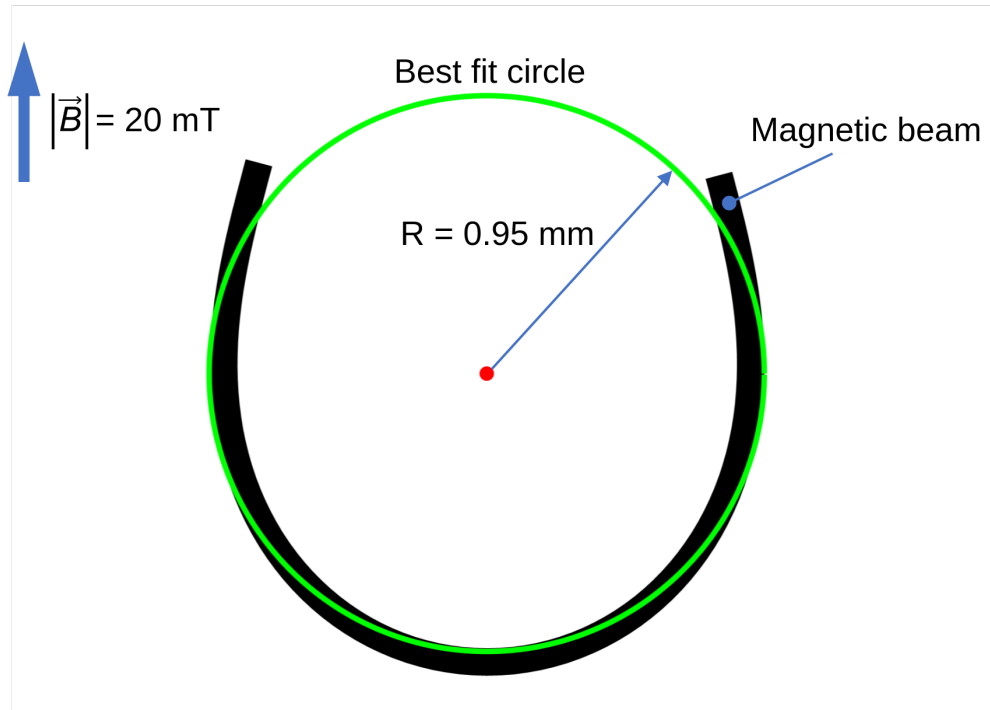


Abbildung 14: Fig. S14. The best fit circle of the rolling MMR during the pick-and-place operations. The shape of the deformed magnetic beam (black thick line) is simulated to determine the best fit circle (green line). The radius of the best fit circle is 0.95 mm.

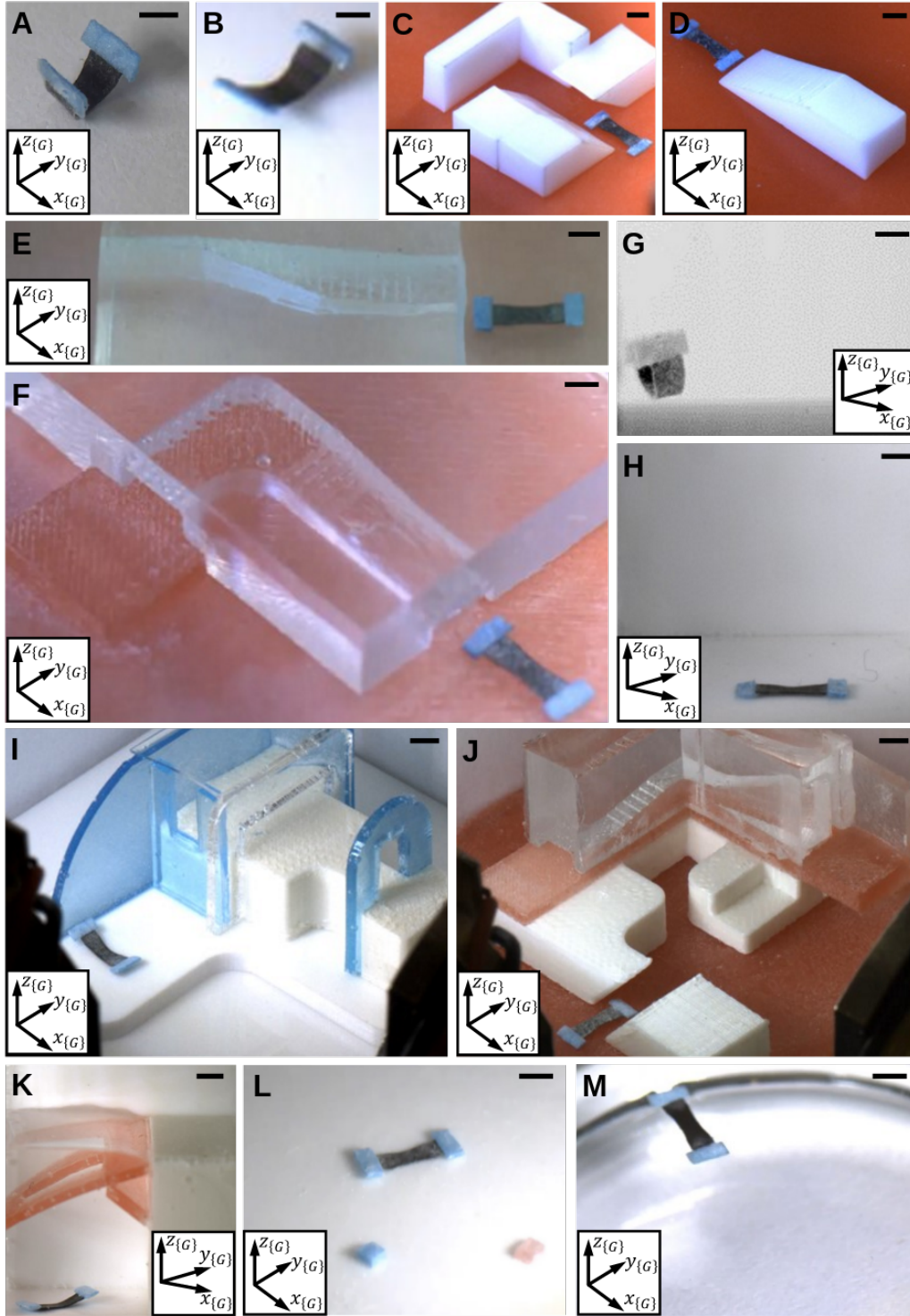


Abbildung 15: Fig. S15. The global reference frame in the experiments shown in SI Video S1-S10. Scale bars: 2 mm.

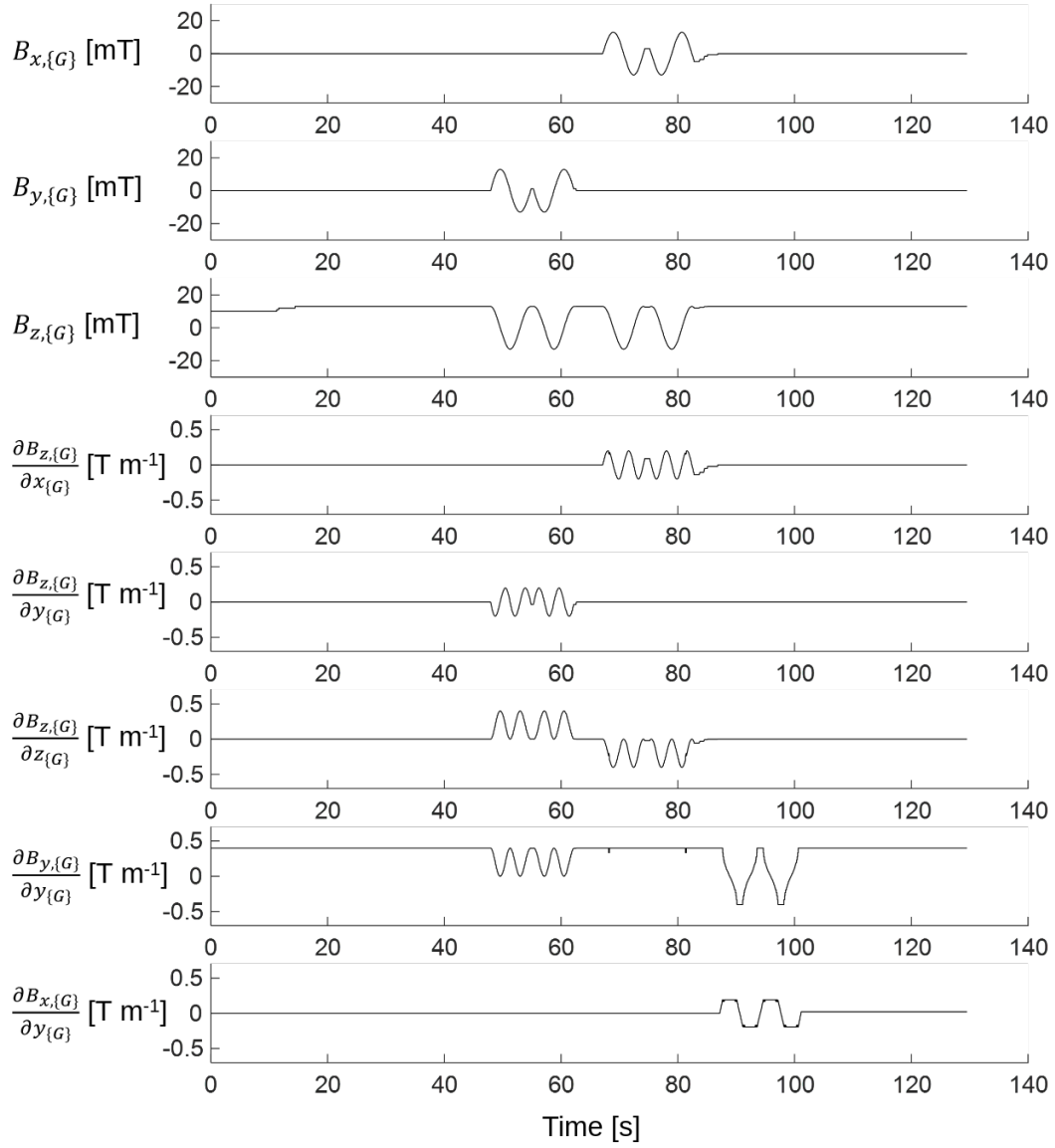


Abbildung 16: Fig. S16. The magnetic actuating signals for the experiment in SI Video S1 (rolling).

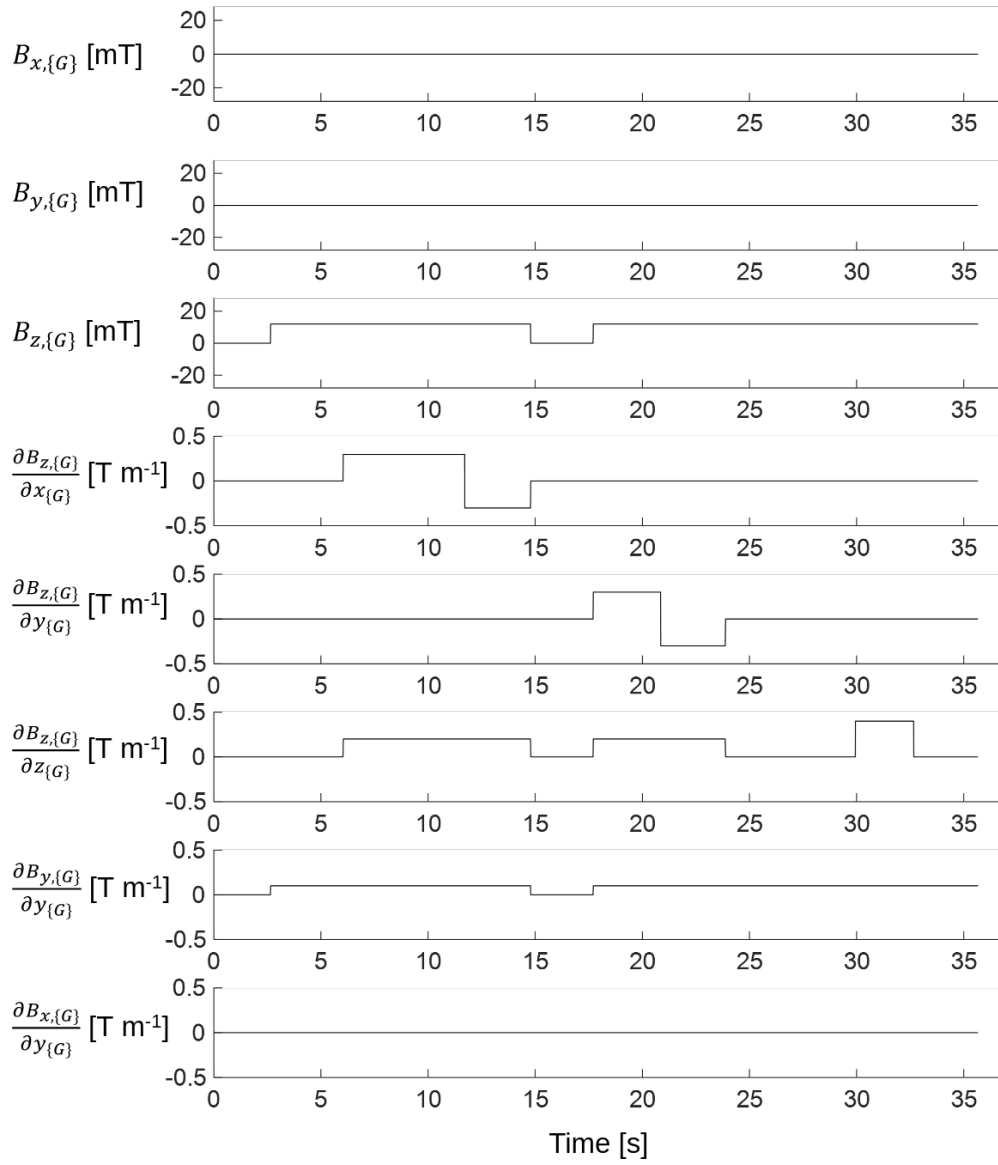


Abbildung 17: Fig. S17. The magnetic actuating signals for the experiment in SI Video S1 (translations).

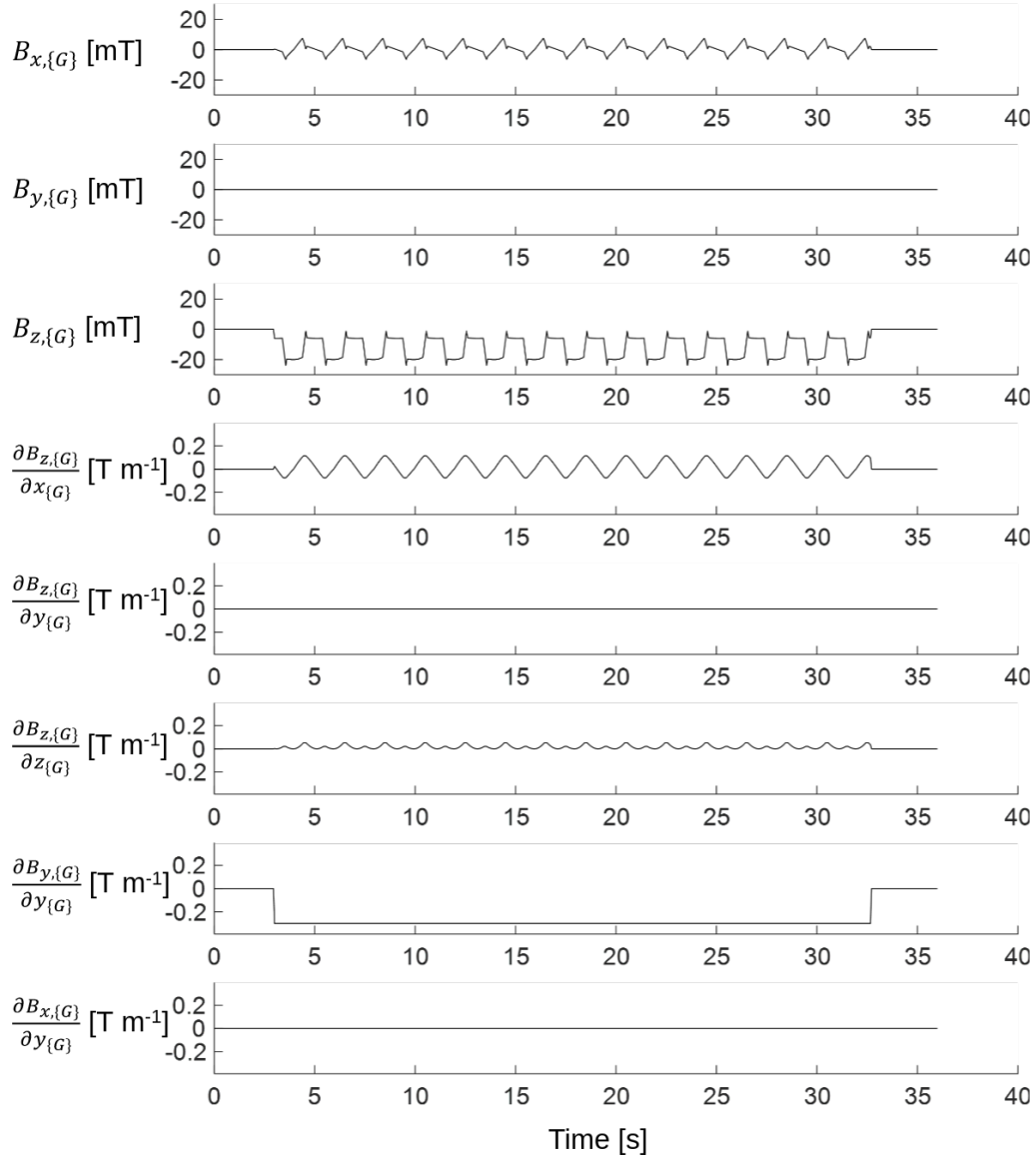


Abbildung 18: Fig. S18. The magnetic actuating signals for the experiment in SI Video S2 (using the two-anchor crawling locomotion to ascend an inclined slope of 20°).

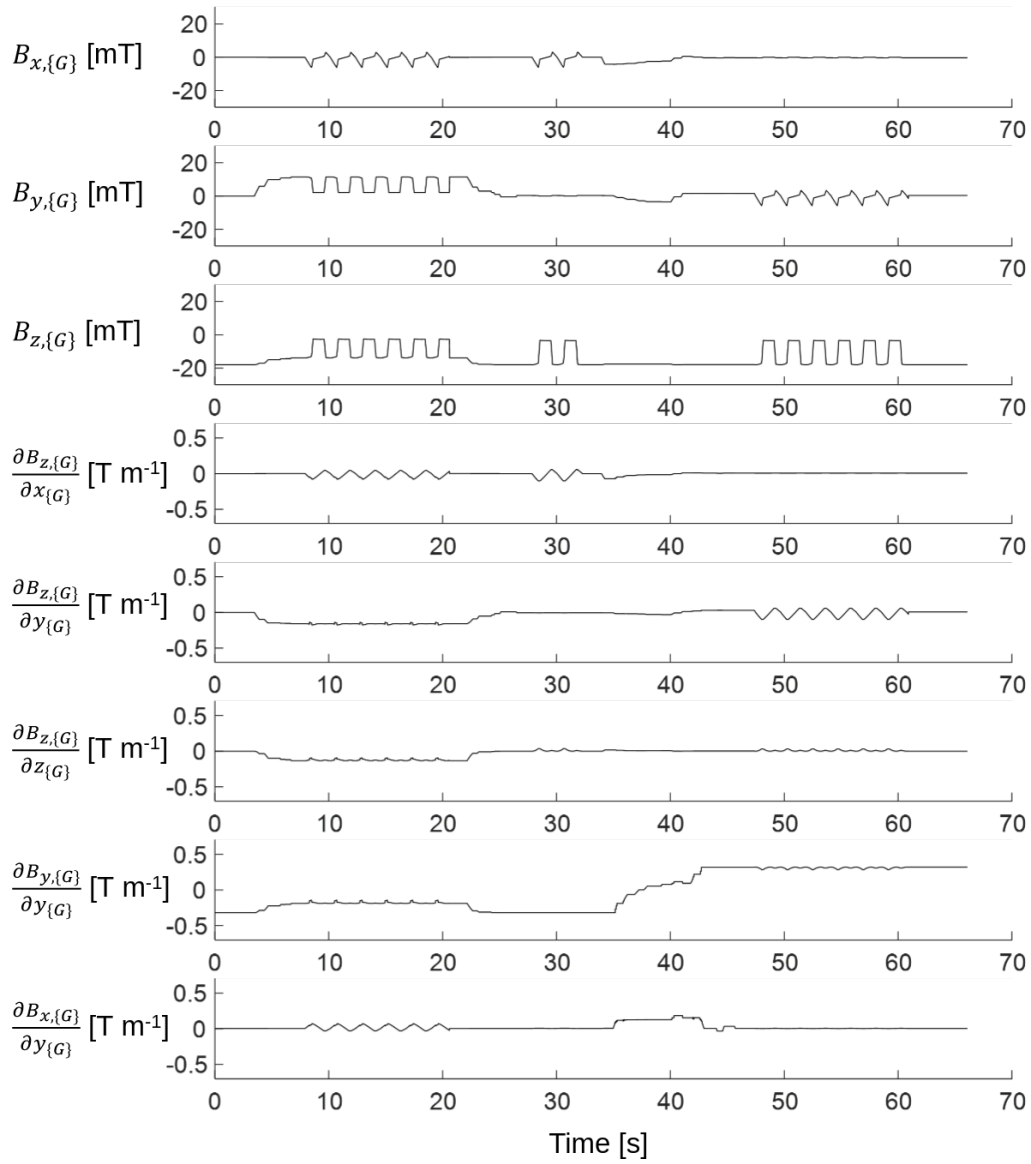


Abbildung 19: Fig. S19. The magnetic actuating signals for the experiment in SI Video S2 (two-anchor crawling across obstacles).

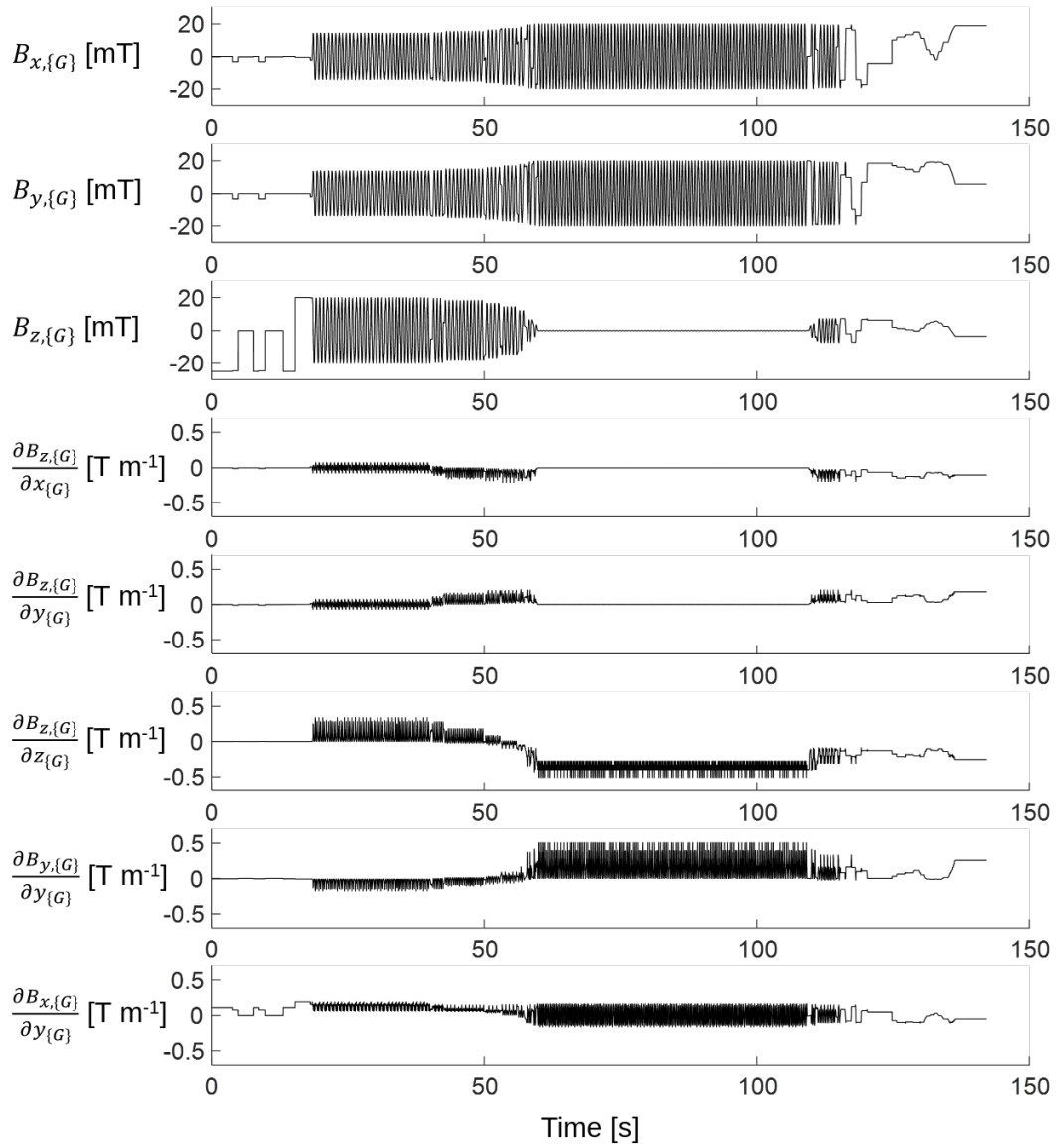


Abbildung 20: Fig. S20. The magnetic actuating signals for the experiment in SI Video S3 (undulating crawling across two perpendicular planes to negotiate a complex channel).

Abbildung 21: Fig. S21. The magnetic actuating signals for the experiment in SI Video S3 (undulating crawling across a complex channel that had an inclined slope of 20° and a sharp turn).

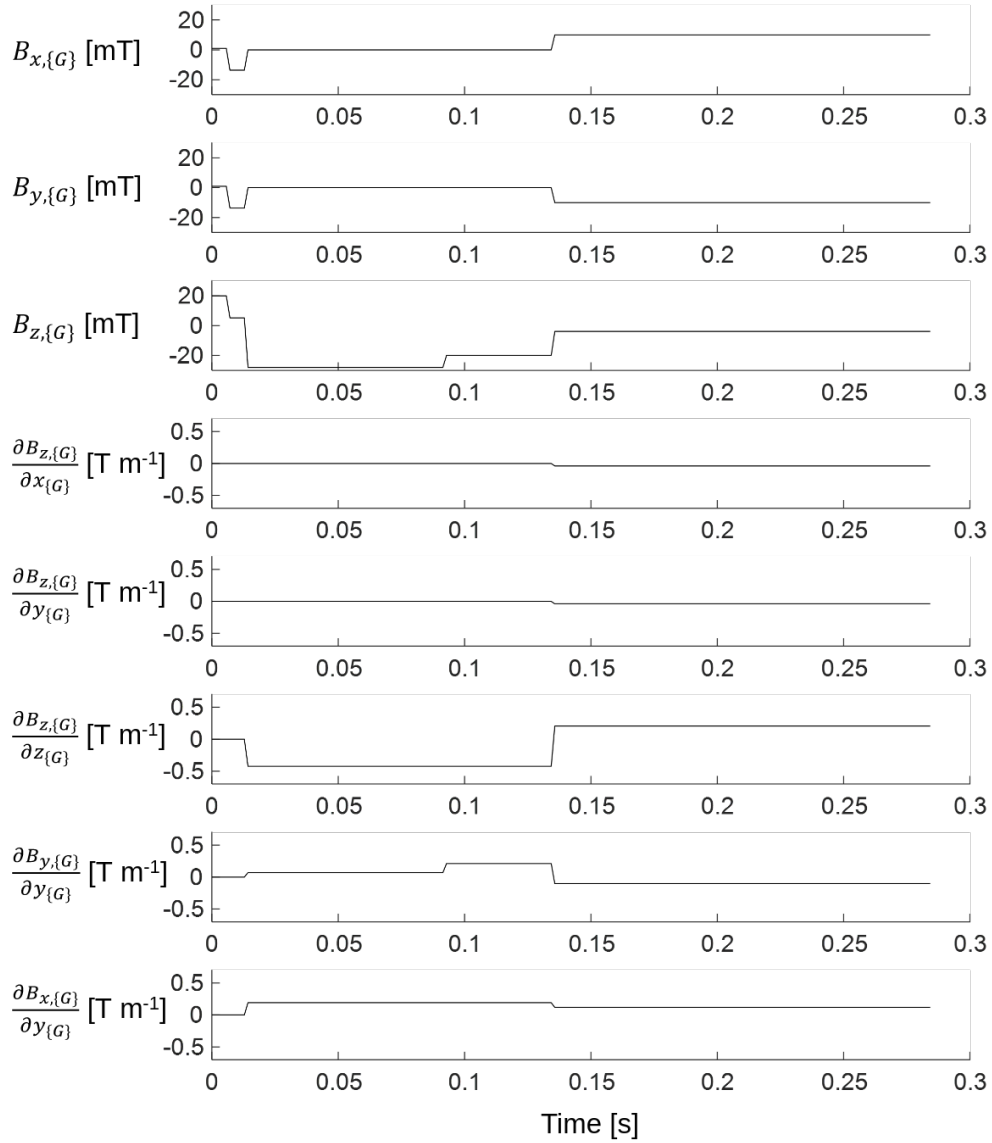


Abbildung 22: Fig. S22. The magnetic actuating signals for the experiment in SI Video S4 (jumping while controlling the angular displacements about the $z_{\{L\}}$ - and $x_{\{L\}}$ -axes of the MMR).

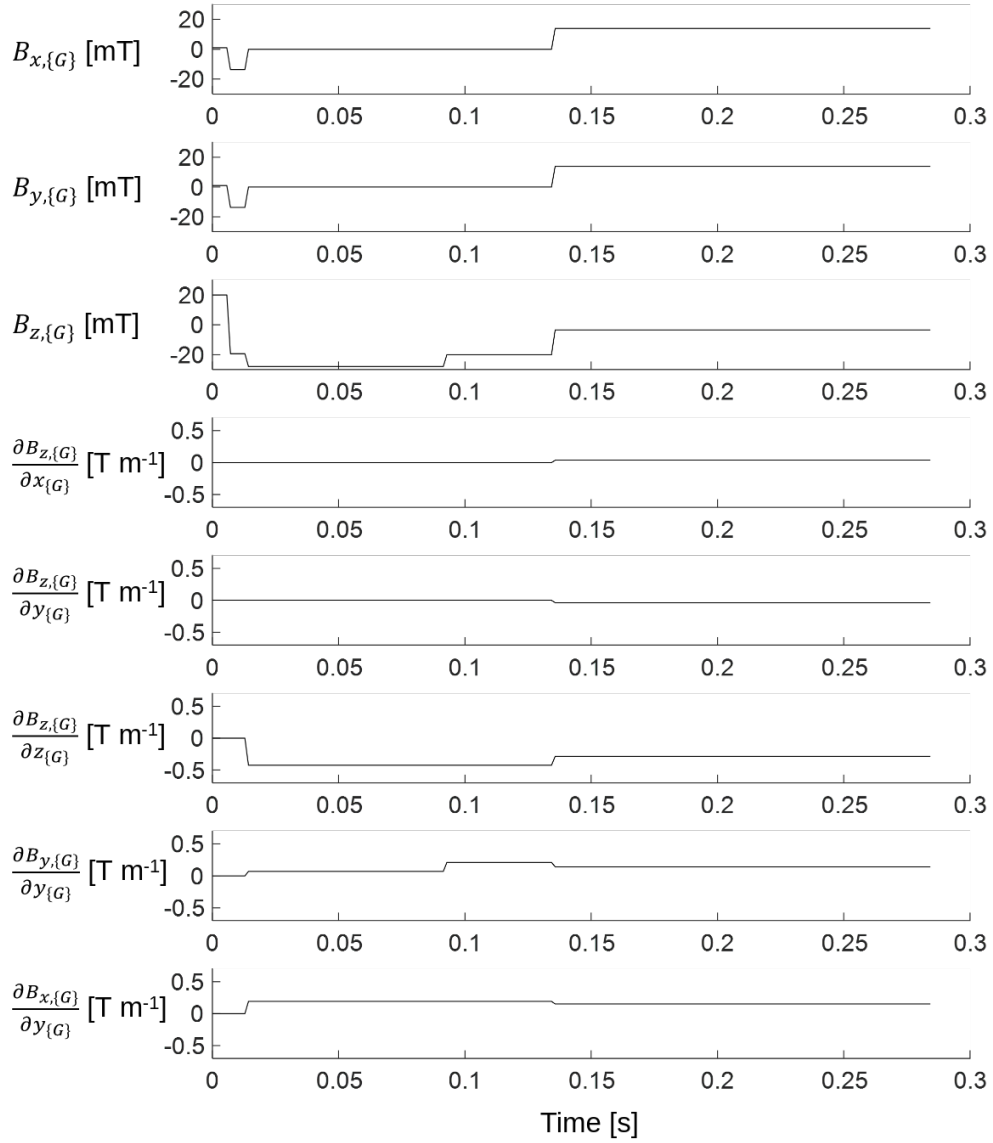


Abbildung 23: Fig. S23. The magnetic actuating signals for the experiment in SI Video S4 (jumping while controlling the angular displacements about the $z_{\{L\}}$ - and $y_{\{L\}}$ -axes of the MMR).

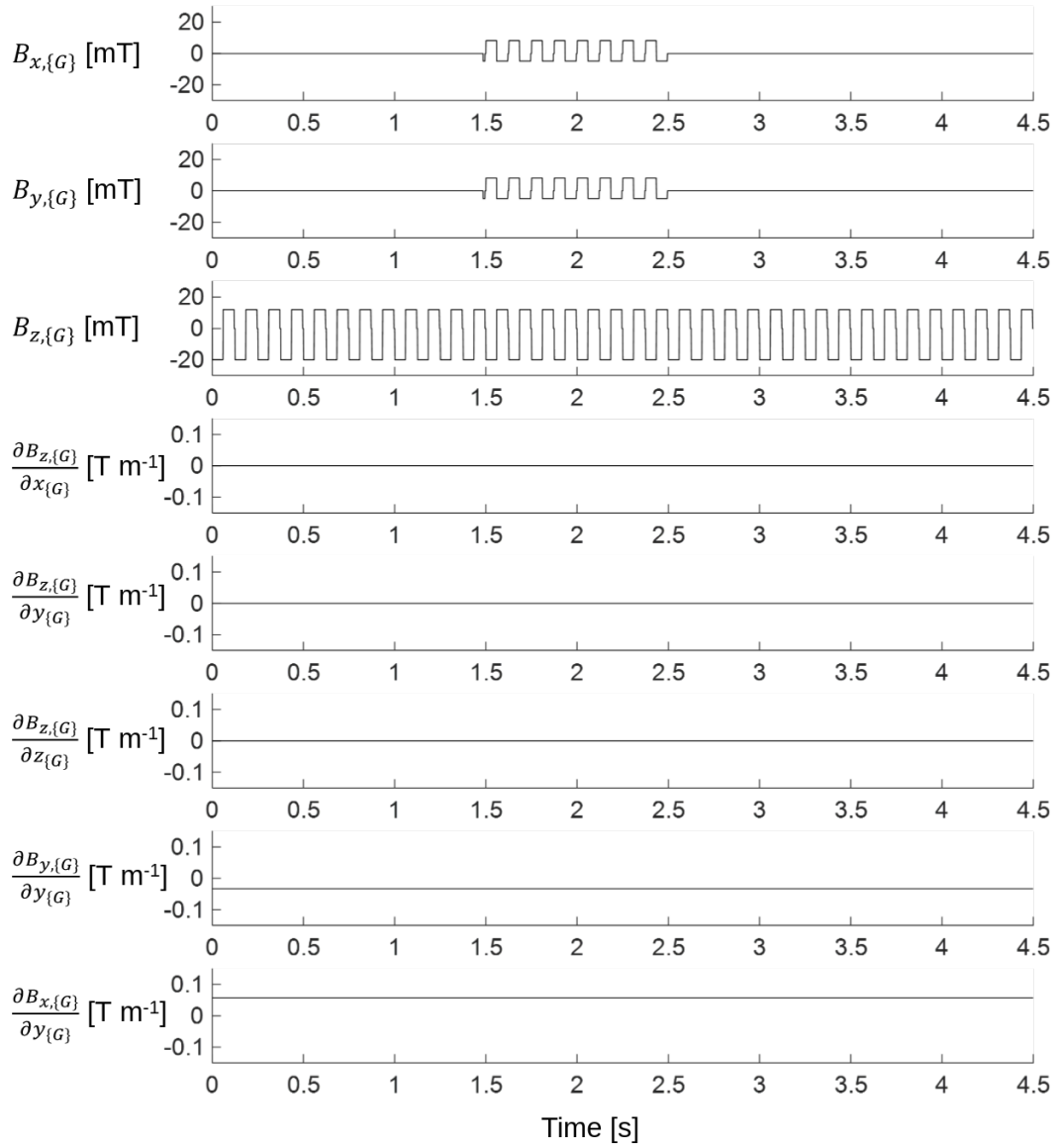


Abbildung 24: Fig. S24. The magnetic actuating signals for the experiment in SI Video S5 (performing the jellyfish-like swimming locomotion while controlling the MMR's $x_{\{L\}}$ -axis rotation).

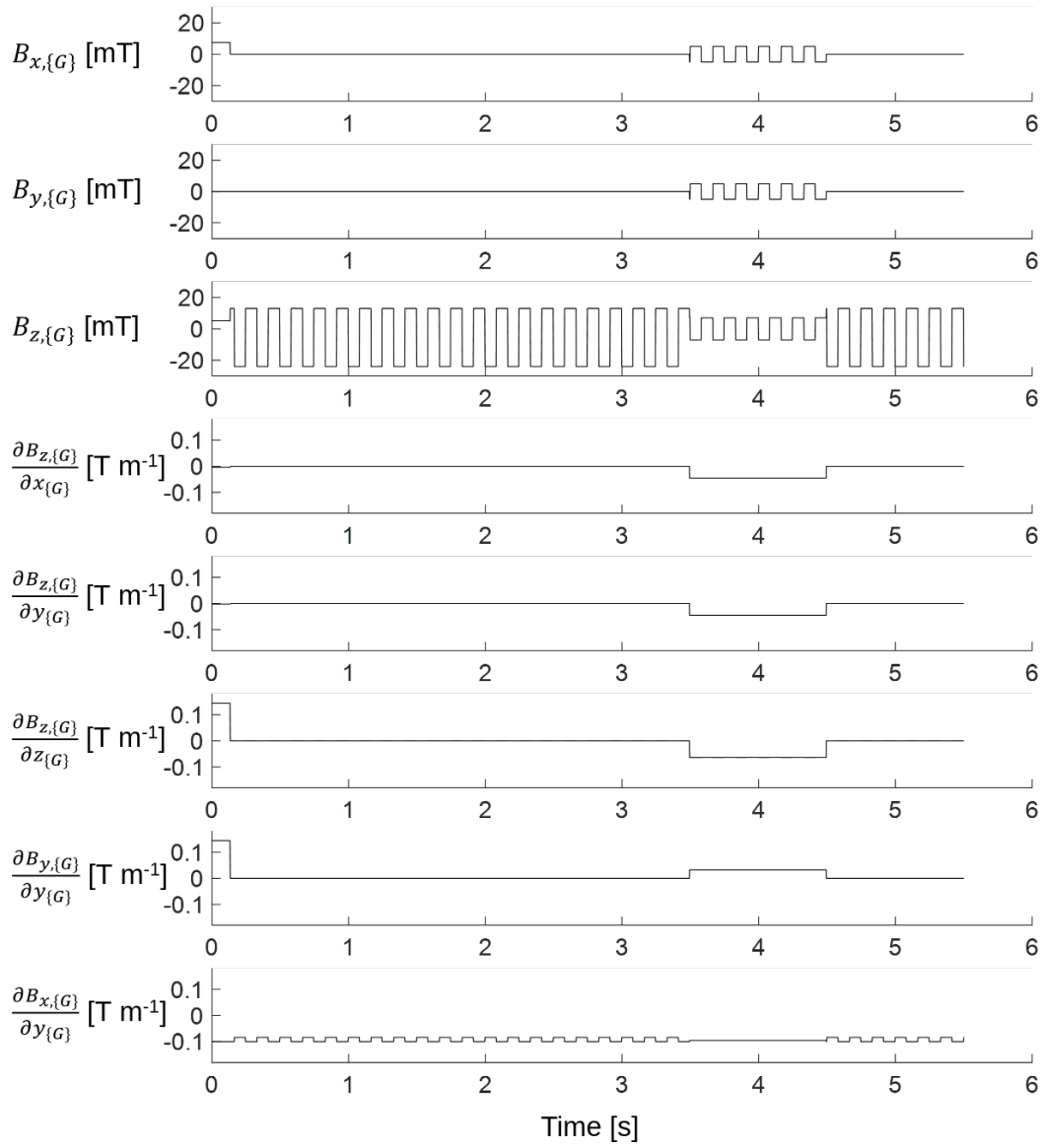


Abbildung 25: Fig. S25. The magnetic actuating signals for the experiment in SI Video S5 (performing the jellyfish-like swimming locomotion while controlling the MMR's $y_{\{L\}}$ -axis rotation).

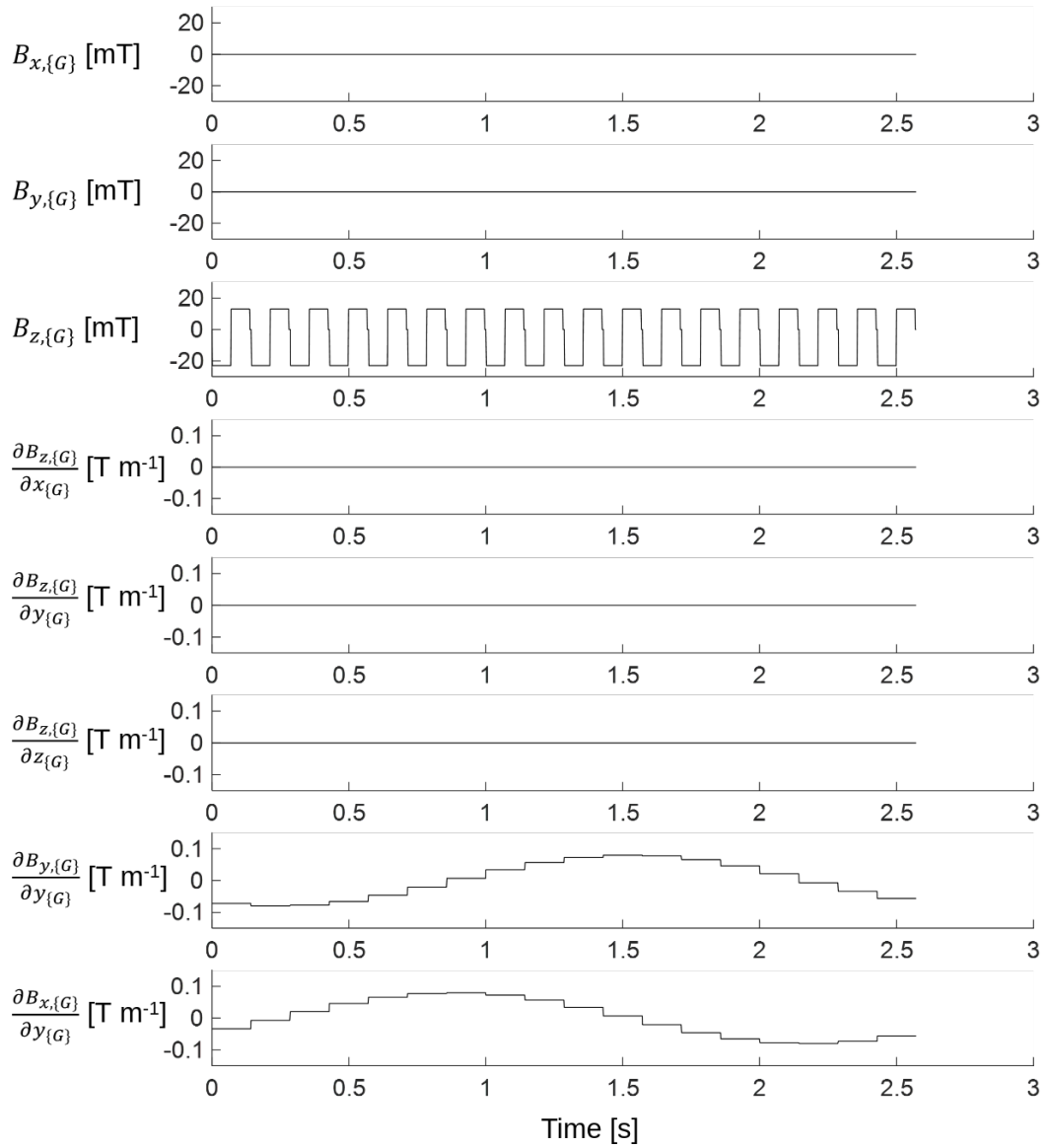


Abbildung 26: Fig. S26. The magnetic actuating signals for the experiment in SI Video S5 (performing the jellyfish-like swimming locomotion while controlling the MMR's $z_{\{L\}}$ -axis rotation).

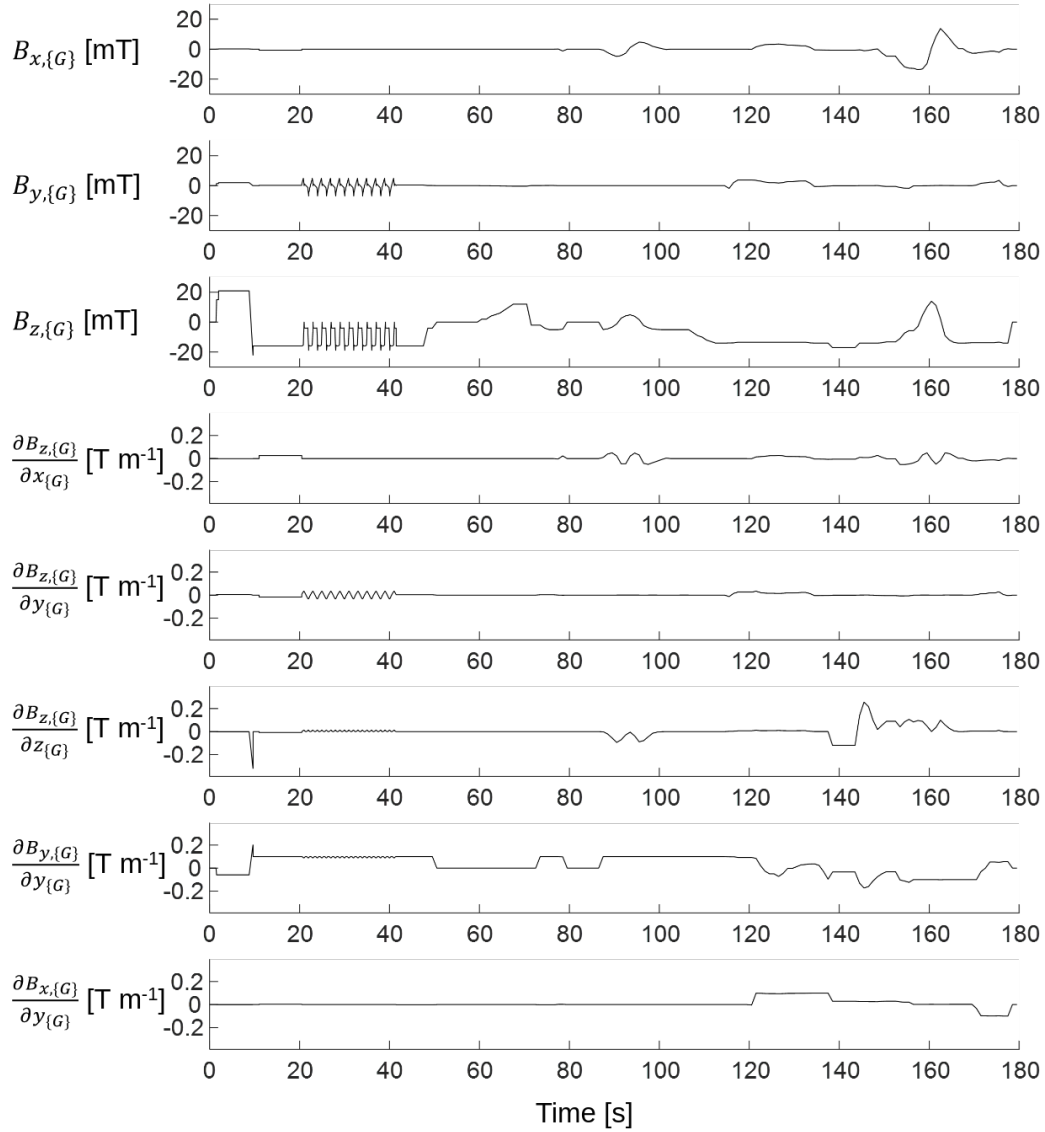


Abbildung 27: Fig. S27. The magnetic actuating signals for the experiment in SI Video S6 (multimodal locomotion: jumping and rolling).

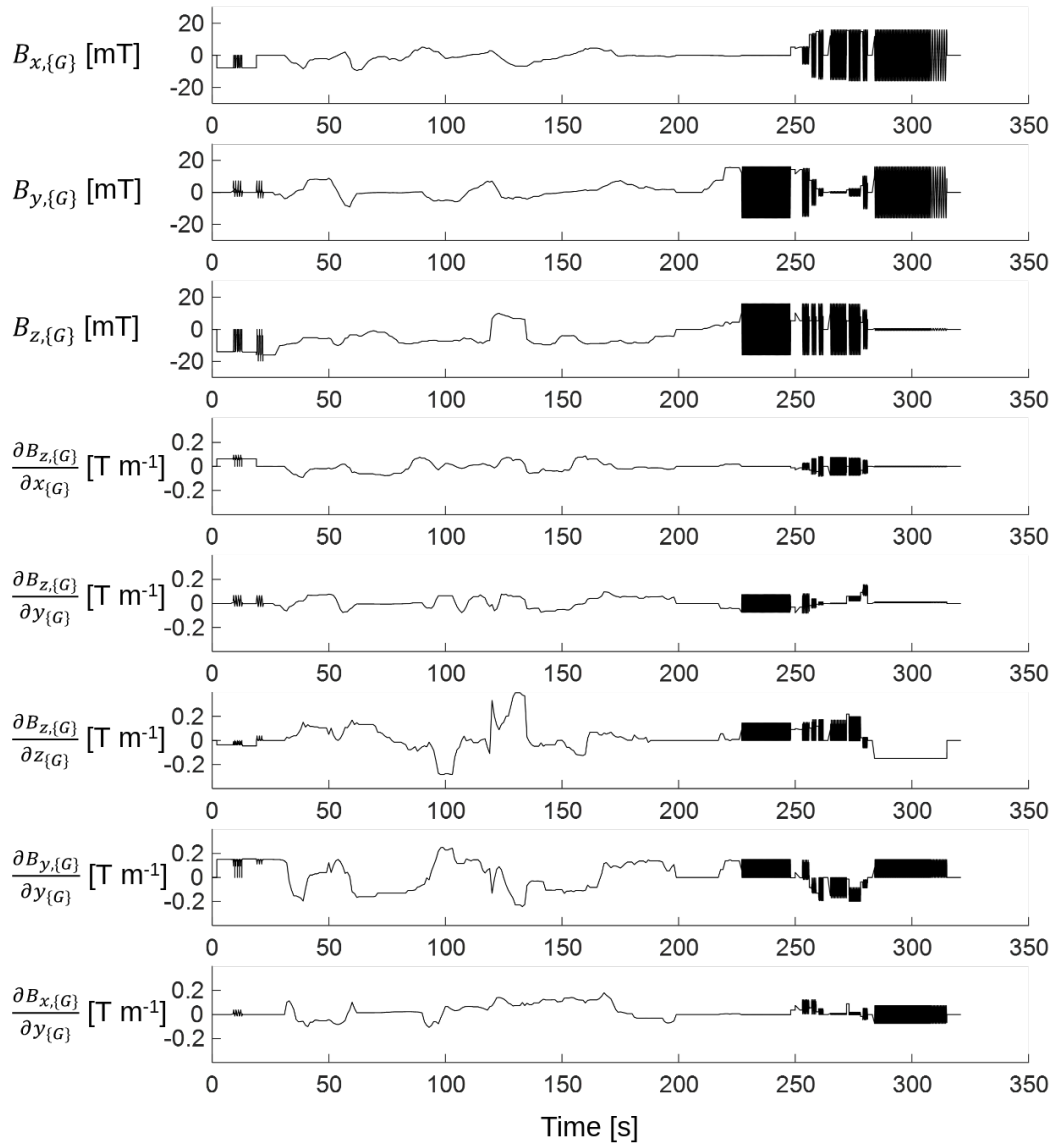


Abbildung 28: Fig. S28. The magnetic actuating signals for the experiment in SI Video S7 (multimodal locomotion: two-anchor crawling and undulating crawling).

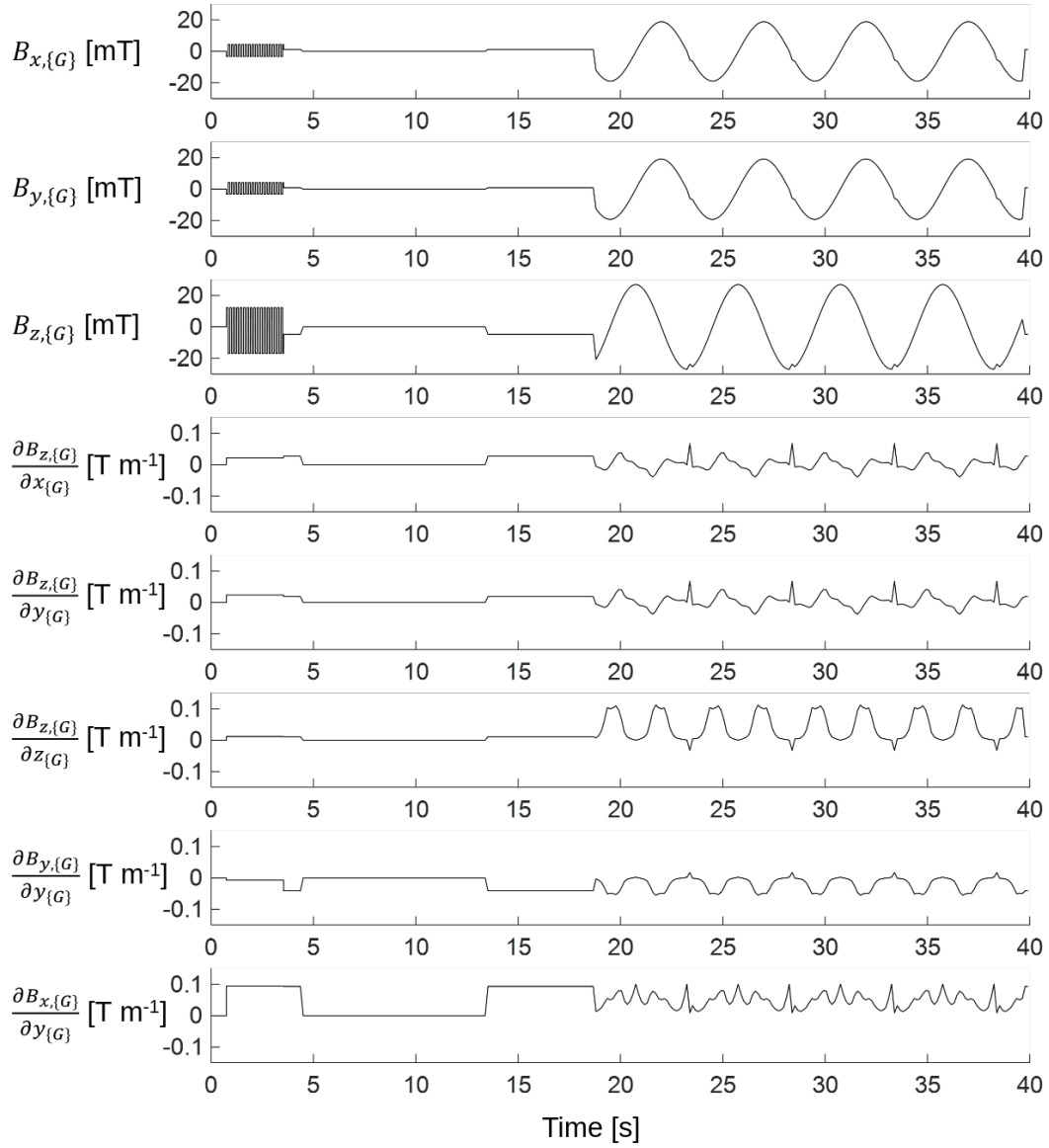


Abbildung 29: Fig. S29. The magnetic actuating signals for the experiment in SI Video S8 (multimodal locomotion: jellyfish-like swimming and landing).

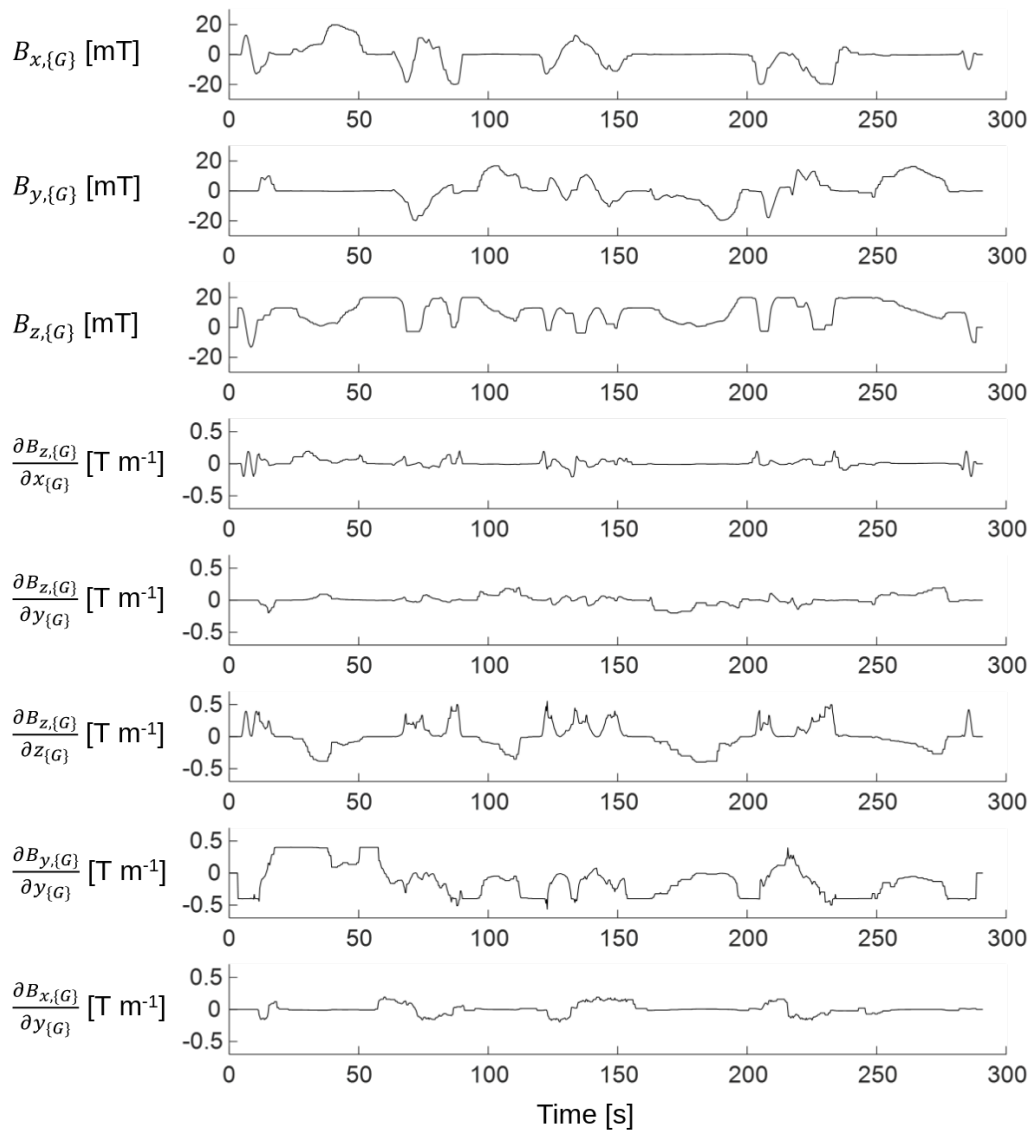


Abbildung 30: Fig. S30. The magnetic actuating signals for the experiment in SI Video S9 (3D pick-and-place operation).

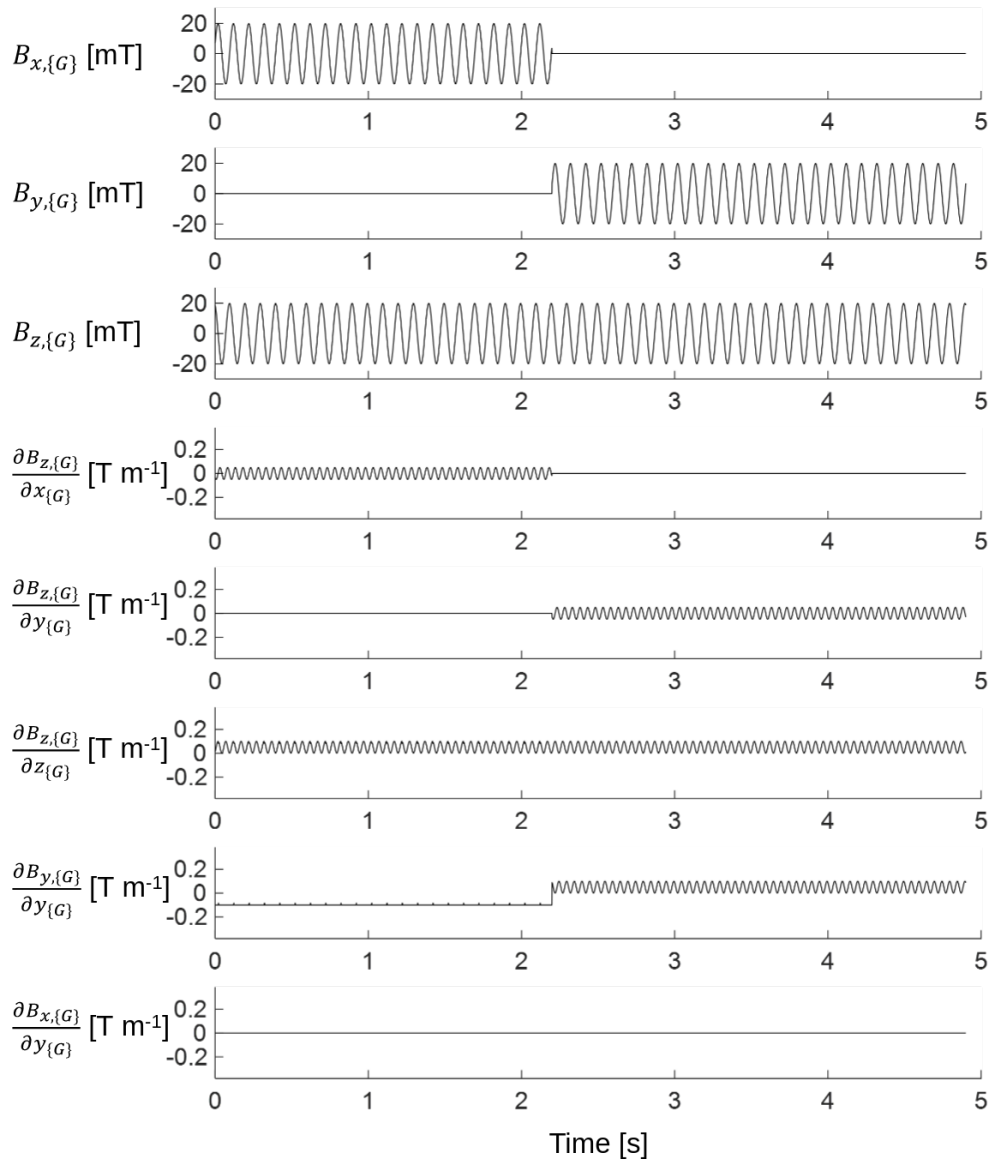


Abbildung 31: Fig. S31. The magnetic actuating signals for the experiment in SI Video S10 (undulating swimming locomotion).

Supporting Table

Table S1. Nomenclature.

Main Text	
\vec{M}	Magnetization profile of the MMR
φ	Phase shift angle of single wavelength harmonic magnetization profile
\vec{m}	Net magnetimoment of the MMR
\vec{B}	The applied magnetidfield
\vec{v}	An arbitrary vector
\mathbf{R}_x	Standard x -axis rotational matrix
\mathbf{R}_y	Standard y -axis rotational matrix
α	The desired angular displacement of the MMR about the $x_{\{G\}}$ -axis
β	The desired angular displacement of the MMR about the $y_{\{G\}}$ -axis
\mathbf{R}_z	Standard z -axis rotational matrix
θ	The desired angular displacement of the MMR about the $z_{\{I\}}$ -axis
\vec{B}_{grad}	The independent spatial gradients of \vec{B}
T_z	The sixth-DOF torque of the MMR
θ_{tip}	Angular deflection at the free end of the fixed-free beam in Fig.2A
Section S1	
L_{sp}	Length of the cuboid samples
w_{sp}	Width of the cuboid samples
t_{sp}	Thickness of the cuboid samples
W	Weight of the cuboid samples
\vec{m}_{sp}	Net magnetimoment of the cuboid samples
\emptyset	Misalignment angle between applied \vec{B} and \vec{m}_{sp}
r_0	Distance between the sample center of mass and anchor point
Γ	The angle between the inclined samples with respect to the substrate
V_{sp}	Volume of the cuboid samples
Section S2	
B_i	Cartesian components of \vec{B} in the i -axis
s	Arclength along the magnetid beam
L	Total length of the magnetid beam
$\tau_{x,\{L\}}$	Magnetid torque distribution in the $x_{\{L\}}$ -axis along the magnetid beam
γ	Rotation deflection angle along the magnetid beam
A	Cross section area of the magnetid beam
M_b	Bending moment along the magnetid beam
E	Young's modulus of the magnetid beam
I	Second moment of inertia of the magnetid beam
V	Volume of the magnetid beam
\vec{T}	Net torque of the MMR
\vec{F}	Net force of the MMR
\vec{r}	Displacement vector from the center of mass of the MMR to a point on its body
\mathbf{D}	The 6×8 design matrix of the MMR

SI Video S1

Rolling locomotion and translations

Rich media available at <https://drive.google.com/file/d/1Fpdx0B0psp6XWmRz3YF9MhgvVChZS1X/view?usp=sharing>

SI Video S2

Two-anchor crawling locomotion

Rich media available at <https://drive.google.com/file/d/15zbajXe3WNx11Ra0QKLjivvbiayIMF5o/view?usp=sharing>

SI Video S3

Undulating crawling locomotion

Rich media available at https://drive.google.com/file/d/1VGC3l_9Abg8G6edJb9QDcpa_pU3owgIM/view?usp=sharing

SI Video S4

Jumping locomotion

Rich media available at <https://drive.google.com/file/d/1btoz2Q53bhX530tsKiGaSlpl8LxhZ7ai/view?usp=sharing>

SI Video S5

Jellyfish-like swimming locomotion

Rich media available at https://drive.google.com/file/d/1jr6sykD4mAAvEuvVFFcBA7oBI_87rQ53/view?usp=sharing

SI Video S6

Multimodal locomotion: Jumping and

Rolling

Rich media available at <https://drive.google.com/file/d/1yf91BYVsvHMY51NtFHmoOE1RPzfVJE9s/view?usp=sharing>

SI Video S7

Multimodal locomotion: Two-anchor crawling and undulating crawling

Rich media available at <https://drive.google.com/file/d/179WATu4KafwUNRCuvyYwDQSa-CHOGAX8/view?usp=sharing>

SI Video S8

Multimodal locomotion: Jellyfish-like swimming and landing

Rich media available at <https://drive.google.com/file/d/1ohZek0JdFFliUTitkPYryV231dgpUkD9/view?usp=sharingew?usp=sharing>

SI Video S9

3D pick-and-place operation

Rich media available at <https://drive.google.com/file/d/12ERhoxl121qVGSd14zNdemUiNgfsi7nN/view?usp=sharing>

SI Video S10

Undulating swimming locomotion

Rich media available at <https://drive.google.com/file/d/1s0ShtycGSgpD22xpXM4mzKi9Db-yT6oS/view?usp=sharing>

References

- Six-degree-of-freedom magnetic actuation for wireless microrobotics. (2016). *The International Journal of Robotics Research*, 35(1-3), 114–128.
- OctoMag: an electromagnetic system for 5-DOF wireless micromanipulation. (2010). *IEEE Transactions on Robotics*, 26(6), 1006–1017.
- Six-degrees-of-freedom remote actuation of magnetic microrobots. (2014). *Robotics: Science and Systems (RSS)*. <https://doi.org/10.15607/RSS.2014.X.013>
- Small-scale magnetic actuators with optimal six degrees-of-freedom. (2021). *Advanced Materials*, 33, e2100170.
- Shape-programmable magnetic soft matter.. (2016). *Proceedings of the National Academy of Sciences*, 113, E6007–E6015.
- Hard-magnetic elastica. (2020). *Journal of the Mechanics and Physics of Solids*, 142, 104045.
- Small-scale soft-bodied robot with multimodal locomotion. (2018). *Nature*, 554, 81–85.

Soft-bodied adaptive multimodal locomotion strategies in fluid-filled confined spaces. (2021). *Science Advances*, 7.

Task space adaptation via the learning of gait controllers of magnetic soft millirobots. (2021). *The International Journal of Robotics Research*. <https://doi.org/10.1177/02783649211021869>

Learning of Sub-optimal Gait Controllers for Magnetic Walking Soft Millirobots. (2020). *Robotics Science and Systems (RSS)*. <https://doi.org/10.15607/RSS.2020.XVI.070>

Continuously distributed magnetization profile for millimeter-scale elastomeric undulatory swimming. (2014). *Applied Physics Letters*, 104, 174101.

Untethered miniature soft robots: modeling and design of a millimeter-scale swimming magnetic sheet. (2018). *Soft Robot*, 5, 761–776.

Millimeter-scale magnetic swimmers using elastomeric undulations. (2015). *IEEE/RSJ International Conference on Intelligent Robots and Systems (IROS)*, 1706–1711.

Independent control of two millimeter-scale soft-bodied magnetic robotic swimmers. (2016). *IEEE International Conference on Robotics and Automation (ICRA)*, 1933–1938.

Viscosity of liquid water in the range 8 C to 150 C. (1978). *Journal of Physical and Chemical Reference Data*, 7(3), 941–948.